Inductive Wireless Power Transfer to Multiple Biomedical Implants

George Alexandrov

Electrical Engineering and Computer Sciences
University of California, Berkeley

Technical Report No. UCB/EECS-2022-10
http://www2.eecs.berkeley.edu/Pubs/TechRpts/2022/EECS-2022-10.html

May 1, 2022

Inductive Wireless Power Transfer to Multiple Biomedical Implants

by

George Alexandrov

A dissertation submitted in partial satisfaction of the

requirements for the degree of

Doctor of Philosophy

in

Engineering - Electrical Engineering and Computer Science

in the

Graduate Division

of the

University of California, Berkeley

Committee in charge:

Professor Jan M. Rabaey, Chair
Professor Rikky Muller
Professor James W. Evans

Spring 2020

Inductive Wireless Power Transfer to Multiple Biomedical Implants

Abstract

Inductive Wireless Power Transfer to Multiple Biomedical Implants

by

George Alexandrov

Doctor of Philosophy in Engineering - Electrical Engineering and Computer Science

University of California, Berkeley

Professor Jan M. Rabaey, Chair

Recent progress in smart devices and the Internet of Things has led to a huge growth in smart systems. Phones, homes, cars, and appliances can all communicate with each other in order to expand their functionality and offer new ways of interaction. Unfortunately, human input/output modalities are still limited to our five senses - sight, hearing, touch, taste, and smell - leading to a gap between humans and the evolving world around us.

The Human Intranet (HI) is the vision that human capabilities will be extended through human-device interaction. It is an open, scalable platform that seamlessly integrates an ever-increasing number of sensor, actuation, computation, storage, communication, and energy nodes located on, in, or around the human body acting in symbiosis with the functions provided by the body itself. A major challenge is providing reliable energy to these devices, as they are inherently distributed and modular, have widely varying energy requirements, and must operate chronically.

This thesis focuses on powering distributed implants inside the body. Two dimensional tessellations of magnetic coils are used to generate a homogeneous magnetic field across a large area and energize implants within. A system for distributed recording of electromyography (EMG) signals in the forearm is presented. Single-channel recording implants located underneath the skin and fat are wirelessly powered through a custom inductive link and transmit uplink data through FDM passive backscatter, enabling chronic EMG recording for use in gesture recognition platforms.

To My Family

Who have always been and continue to be there for me in every way

Contents

List of Figures

List of Tables

Acknowledgments

First and foremost, I need to thank my advisor, Professor Jan Rabaey. Jan, you provided guidance when needed, but for the most part allowed me to explore what I found interesting, and this was a huge component of why I had such an amazing experience at Berkeley. I am incredibly grateful to have been able to spend seven years working with you. Special thank you also to Professors Rikky Muller, Elad Alon, Jose Carmena, Michel Maharbiz, Ana Arias, and James Evans for discussions and guidance.

My parents Peter and Siyka, thank you for all of the support you have provided throughout my life, and especially over the past seven years. Every sacrifice you made and hardship you faced has helped me get to where I am today, and for that I am eternally grateful.

My brother Boris, thank you for leading the way in everything. In ways big and small, I have followed in your footsteps my whole life and emerged a better person. Thank you also to my sister in law Aarti for the countless words of wisdom.

To my wife Maren, thank you for supporting me mentally, emotionally, physically, and to some extent financially through my PhD. I could not do this without you.

My group mates - Ali, Andy, Matthew, Alisha - thank you for the advice, help, collaborations, and distractions. I have learned a lot from each of you and wish you all the best in wherever life takes you next. Thank you also to various former Jan group members - Nathan, Will, Dan, Jackie, DJ - for warmly welcoming me to the group. Thanks also to Benjamin Johnson for help with OMNI and WAND testing, Samantha Santacruz for help in the monkey lab, and of course Mario and Luigi.

Thank you to the revolving cast of Jan's visitors - Alba, Alvaro, Arno, Flavien, Geovane, Guillaume, Robin, Simone, and Stijn. Thank you also to the rest of the BWRC students - Keertana, Emily, Bonjern, Seobin, Nima, Lazar, and everyone else with whom I shared a meal, an idea, or a joke.

I would like to thank all of the BWRC staff. Candy, thank you for doing so much around the center and for being a great friend. If Ajith is reading this, Candy deserves at least a 100% raise. Thank you to James, Fred, and Brian for engineering and lab support - the center would not run without you! Thank you to all of the administrative staff at BWRC and Cory - Shirley, Mikaela, Olivia, and Amber.

Last, but certainly not least, thanks to all of my friends who have talked to me about this PhD, provided support, and most importantly been a welcome distraction from academic life. Joey, Dan, Alexa, Mike, Sara, Andy, Matt, Aharon, Esthena, Nicole, Ana Karen, Jessie, Bill, Gena, Vivian, Basil, Grace, Sasha, Aaron - thank you all.

Chapter 1

Introduction

Biomedical implants have proliferated in part due to advances in electronics, materials, and medicine which combine to create devices that are smaller, less invasive, more biologically compatible, more intelligent, and more useful. The recent rise in aging populations has also increased the demand for biomedical implants. According to the UN, the percentage of the global population over the age of 65 has increased from 5% in 1950 to 9% in 2020 and is expected to reach 16% by 2050 [1]. During the same time frame (1950-2020), life expectancy increased from 47 to 72.6 years and is projected to reach 76.8 by 2050. As people live longer thanks to access to advanced medicine, better diets, and an overall healthier lifestyle, organ failure is common and neurological disorders have more time to develop, thus necessitating more medical devices to address these health issues.

Biomedical implants have a long history and range from purely mechanical devices such as stents and artificial hips to advanced electromechanical systems like neurostimulation devices and insulin pumps. This thesis focuses on active implanted devices which require a continuous source of energy to operate internal electrical and/or mechanical systems. In particular, the main goal of this work is to explore a methodology for powering future biomedical implants as new paradigms emerge. Unlike traditional implanted devices, future devices will be miniaturized and distributed in order to address disorders and conditions at the system level [2], and therefore require novel powering techniques.

1.1 The Human Intranet

The Human Intranet (HI) (Figure 1.1) is envisioned as an open and scalable platform for human-device interaction through a combination of sensors, actuators, energy storage, computation, and communication nodes in, on, or around the body working to extend human capabilities beyond the basic senses of sight, touch, smell, hearing, and taste [3]. It is a chronic, distributed, and intelligent network of devices with vastly different energy requirements, whose goal is to replace, repair, or add new inputs or outputs to the human body. Some devices, such as an advanced prosthesis, may require a large amount of power for its

various motors and actuators and include a large energy source in the form of a battery. On the other hand, smaller implanted devices like neurostimulators or biophysical recording nodes are by design low-power devices, and therefore do not require large amounts of energy to operate. However, these devices are typically size-constrained as well as energy-constrained and chronic operation must be guaranteed through reliable energy delivery, for example an implanted battery or via a transcutaneous wireless power link.

Figure 1.1: The Human Intranet concept, from [3].

Realizing the HI vision requires devices which are miniaturized, distributed, and modular, unlike traditional in-/on-body devices, a few examples of which are shown in Figure 1.2. These, like most typical commercial and FDA-approved implanted devices, consist of a central implant containing the circuitry required for recording and/or stimulation, and long subcutaneous leads which are used to access distant physiological features for recording and/or stimulation. This design is a reasonable tradeoff among packaging, implantation complexity, and spatial coverage.

There are three primary methods of energizing such an implanted system which are currently used commercially: via an implanted energy source (e.g. electrochemical battery) which is designed to power the device for its entire lifetime, via an implanted energy source which requires wireless recharging, typically accomplished with an inductive link, or via continuous wireless powering, again typically via an inductive link. These inductive wireless power transfer (WPT) links consist of a pair of coils (one implanted in the device, the other outside of the body) and require precise alignment to ensure high efficiency and safe, reliable operation of the implant.

Many other method of powering implants exist and have been demonstrated under experimental conditions, but few are deployed in an FDA-approved device. These are outlined

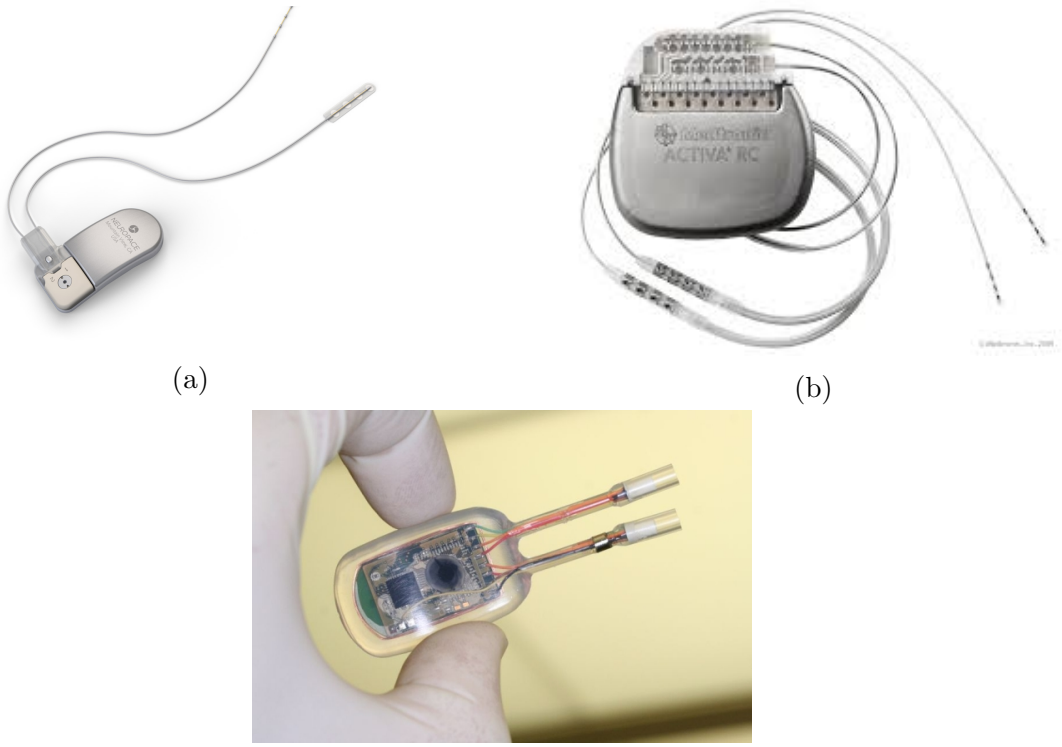

(a) (b) (c)

Figure 1.2: A few traditional biomedical implants. (a) Neuropace RNS stimulator, (b) Medtronic Activa RC neurostimulator, and (c) Myoplant implanted EMG recording system. Images courtesy of [4, 5, 6].

in Table 1.1. Batteries are a common method of powering implanted devices, but have a limited lifetime and require replacement necessitating surgery or other invasive measures [7]. They are most commonly found in low energy devices such as pacemakers which can operate for tens of years without requiring service. Other methods of powering implants such as bio-fuel cells, thermoelectric generators, or RF harvesting suffer from low output power and cannot generate enough energy to power sophisticated implants such as neurostimulators [8]. However, as implants continue to decrease in size and energy, these options may become feasible.

The devices required to enable HI would be miniaturized, distributed, and numerous, potentially spanning the entire body and having different energy requirements, and powering each device with a dedicated external coil is impractical, particularly as the numbers of implants grows. This thesis proposes a novel method for powering distributed implanted nodes within the body and considers electromyography (EMG) as one potential application for this within the constraints of HI.

Energy source	Approximate power density	Advantages	Disadvantages
Battery	1 mW h/mm^3 [7]	Simple	Limited lifetime
Bio-fuel cell	0.01 µW/mm^3 [9]	Biocompatible	Limited lifetime Low output power
Thermoelectric	0.1 µW/mm^3 [10]	Unlimited lifetime	Low output power
Ultrasound	100-500 µW/mm^2 [11, 12]*	Deeper penetration Less tissue loss Higher power density for implant sizes below 1 mm	Low power High loss through bone
Inductive	1-100 mW/mm^2*	High power	Tissue absorption Low power density for implant sizes below 1 mm

* depends on separation between external TX and implant

Table 1.1: Powering options for biomedical implants, partially adapted from [8].

1.2 Chronic Electromyography as an Application for the Human Intranet

Electromyography (EMG), the recording of the electrical activity of muscles, is an easily accessible physiological signal containing information about underlying neural and muscle activity. It has seen use in a wide variety of applications including gesture recognition [13], human-machine interfaces [14, 15], advanced prostheses [16], and medical diagnoses [17]. These applications require high channel count and spatially diverse recordings in order to capture the wide array of possible movements [18]. Moreover, these systems rely on continuous EMG recording and therefore require an unobtrusive recording platform which can be used chronically without user fatigue or discomfort.

A chronic EMG system such as this may be part of a larger HI system for restoring limb functionality in an amputee in the near future. This system may include a neural implant in the motor cortex or somatosensory cortex, a series of implanted EMG-recording nodes in the residual limb, and an external prosthetic arm. Each component of the system works in tandem to restore functionality to the user, in this case the ability to manipulate the prosthetic arm and restore haptic perception. It accomplishes this by combining neural data recorded from the motor cortex with EMG data from existing muscles in order to predict movement intentions and translate these to control signals for generating the appropriate movement at the prosthesis, for example as in [19]. Crucially, such a system needs to operate chronically in order to seamlessly integrate the technology with daily life, so each component

needs to be powered reliably and chronically.

The precise method of powering each component can vary and is usually determined by size, energy, and safety constraints. The prosthetic arm is large, external, and contains powerful motors which require relatively large amounts of energy, so a large secondary (rechargeable) battery is best suited. However, both the neural implant and the EMG-recording implants are implanted and size constrained and require a different method of energy delivery. Traditional options for powering such implanted devices include implanted batteries, implanted bio- and thermo-electric generators, ultrasound, or electromagnetic coupling [8]. The exact choice is determined by various factors including the implant size, implant depth, power dissipation, and operational lifetime, but the most widely used method is inductive power transfer from an external coil to the implant in order to provide continuous energy or recharge an implanted energy source. These systems are widely used and well studied and can provide tens of mW of power through millimeters to centimeters of tissue.

However, inductive links rely on precisely co-designed coils which require precise spatial alignment in order to achieve high power transfer efficiencies and deliver enough energy under safety constraints, making them unsuitable for a distributed system such as the EMG-recording nodes in the example in this section. These nodes are distributed, miniaturized, and modular in order to be able to record from a large number of muscles with a large spatial coverage, as needed by prosthesis control applications [18]. Requiring a dedicated external coil for each implant and maintaining long-term alignment is infeasible from a design standpoint. Thus, a different powering modality is required to provide reliable energy across a large surface to multiple, randomly distributed, miniaturized implants.

This thesis proposes a platform for powering multiple, randomly distributed implants through inductive WPT. It consists of two dimensional tessellations of individually optimized inductive coils which are arrayed in such a way as to generate a constant magnetic powering field in the location of the implants. This thesis presents a design methodology for designing these WPT links by first optimizing individual inductive sub-coils and providing guidance on the best methods of arraying them to achieve large spatial coverage while maintaining high system efficiency and good homogeneity. This multi-coil WPT link is used to power a number of single-channel recording EMG nodes designed as part of a chronic system for EMG recording. Simulation results and measurements are presented throughout to validate functionality and explain important design criteria.

1.3 Thesis Outline

The thesis is organized as follows:

Chapter 1 provides background and motivation on the Human Intranet (HI) with a focus on powering complex and distributed HI systems. Requirements for HI devices and techniques for powering these systems are discussed. A chronic EMG-recording platform is introduced as a guiding example for powering a HI system.

Chapter 2 begins with a history of inductive wireless power transfer with an emphasis on medical and implanted applications. A derivation of the efficiency of a standard two-coil link is presented, followed by a discussion of methods for maximizing this efficiency in biomedical implants. The chapter concludes with a design methodology for maximum efficiency two-coil inductive links.

Chapter 3 extends the principles of designing high efficiency two-coil links for powering multiple devices. A generic structure is proposed consisting of a one or three layer, two-dimensional tessellation of hexagonal sub-coils for powering randomly distributed biomedical implants. The tradeoffs among efficiency, homogeneity, and driving complexity are discussed and illustrated through simulations.

Chapter 4 describes the EMGnode system for chronic recording of subcutaneous EMG. The system architecture is described, which includes a miniaturized, low-power, and discrete implant containing an analog front-end for EMG recording, inductive wireless power transfer link, and passive backscatter for uplink data transmission. The chapter also details the design of a wireless power transfer link for multiple, randomly distributed EMGnode implants in the forearm using the coil design of Chapter 3. It includes simulation and measurement results for the EMGnode implant as well as the inductive power link which provides homogeneous energy to multiple randomly distributed EMGnode implants.

Finally, Chapter 5 summarizes the contributions of this thesis and proposes possible extensions and improvements of this work.

Chapter 2

Inductive Wireless Power Transfer

Inductive power transfer is the oldest form of wireless power transfer, with systems for transferring energy through inductive means reported since the early 1900s for powering light bulbs and other basic electronics. Since then, inductively coupled power transfer has seen uses in disparate fields such as electric vehicles [20], consumer electronics [21], and medical devices [22], owing to the wide variety of power densities, high efficiency, and safety. In the 1960s, the first system for inductive wireless power transfer to a medical implant was developed for an artificial heart [23], paving the way for a variety of wirelessly powered biomedical implants with smaller sizes, higher power efficiencies, and more sophisticated fabrication methods [24, 25, 26].

Regardless of the size and shape of the individual coils and the particular application, inductive wireless power links operate in the near-field and transfer energy through an alternating magnetic field generated by a transmitter coil (Figure 2.1). The transmitter (TX) coil is driven with an alternating current (AC) I which generates an AC magnetic field B according to Ampere's Law:

$$\oint_C \boldsymbol{B} \cdot \, dl = \mu_o \iint_S \boldsymbol{J} \, d\boldsymbol{S} = \mu_o I \tag{2.1}$$

where J is the current density, μ_o is the magnetic constant, and dl and dS are infinitesimal elements of the curve and surface of the current, respectively. A portion of this magnetic field is captured by the receiver (RX) coil and induces an AC voltage V_{ind} in accordance with Faraday's Law:

$$V_{ind} = \oint_\Sigma \boldsymbol{E} \cdot \, d\boldsymbol{l} = -\frac{d}{dt} \int_\Sigma \boldsymbol{B} \, d\boldsymbol{A} \tag{2.2}$$

where E is the electric field and Σ is the surface through which the magnetic field flows through. which shows that the generated voltage is directly proportional to the changing magnetic flux through the coil. This induced voltage is rectified and used to generate a steady power supply to power any electronics on the secondary, for example to charge a battery or power a stimulator.

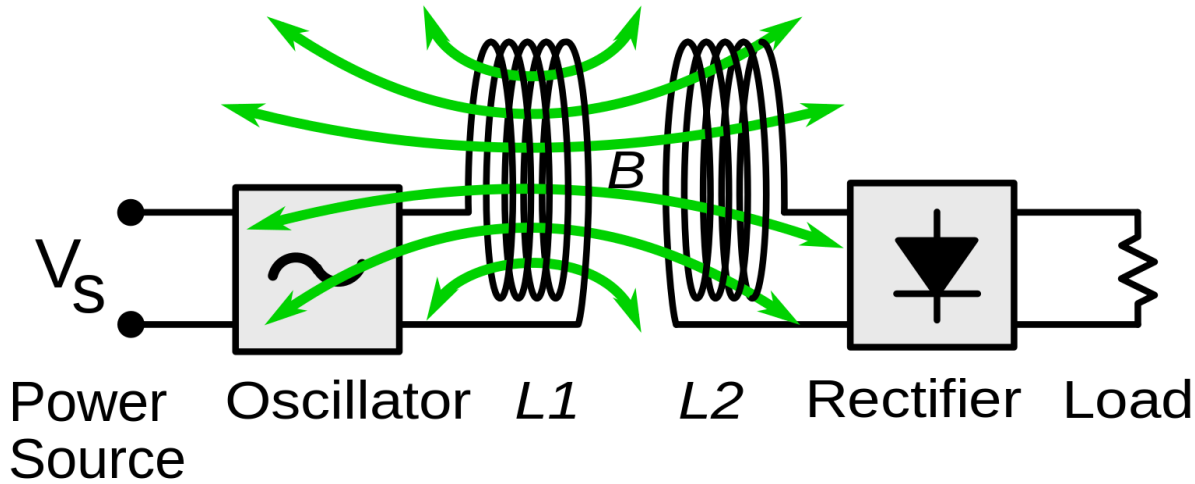

Figure 2.1: Generic block diagram of inductively coupled wireless power transfer. Power is transferred from an energy source (Vs) through air or other media via an alternating magnetic field generated by a primary coil. This energy is received and rectified by a secondary coil in order to power a load. Image courtesy of [27].

From eq. (2.1) and eq. (2.2), it is evident that the power transfer capability of an inductive WPT link can be improved by:

a) increasing the magnetic field strength (e.g. by using a TX coil with large number of turns);

b) increasing the drive current of the primary;

c) increasing the rate of change of magnetic flux (e.g. by increasing the frequency of I);

d) increasing the amount of magnetic flux coupled to the secondary (e.g. by reducing the TX-RX separation and guaranteeing axial alignment);

e) adding a ferromagnetic core.

Typically, inductive WPT links are designed to deliver a minimum amount of power at a pre-determined distance with maximum efficiency, given physical constraints on the TX and/or RX coil. Important parameters include power delivered to the load (PDL), power transfer efficiency (PTE or η), and operating range, and depend on various system characteristics including coil geometry, coil separation, coil alignment, frequency, impedance matching, and intervening media, to name a few. The coil geometry and separation determine the magnetic coupling k between the coils, which is a primary determinant of the

overall system efficiency. Usually some of the parameters are constrained by the particular application, namely the size and shape of the implanted coil and minimum separation.

Improving the WPT capabilities based on the five metrics outlined above is not always feasible due to system and physical constraints. For example, increasing the number of turns of the TX coil increases the magnetic field strength, but also increases parasitic capacitance due to inter-winding interactions which lowers the self-resonance frequency (SRF) of the TX. Increasing the TX current is a commonly used technique to transfer higher amounts of power, but increases I^2R losses at the TX and can lead to harmful heat generation near the skin and exceed other safety factors related to permanent tissue damage. Increasing the operating frequency is another technique which has been shown to improve WPT efficiency specifically for small and/or deep implants [28, 29], but this technique is limited due to increased tissue interactions at higher frequencies leading to an increase in the specific absorption rate (SAR), and limitations on coil SRF. Finally, increasing the magnetic flux coupled to the RX by reducing the distance is usually not possible due to physical and system limitations. Biomedical implant depth is determined by the application and is usually not a design parameter, so the TX-RX distance is limited to a minimum of the tissue thickness between the implant and the skin interface.

Recently, there has been a tremendous increase in the number of electronic systems in, on, or around the body [3]. Advances in electronics miniaturization, materials, and low power design have led to the development of chronic implanted systems for sensing and/or actuation within the body. A primary challenge for such systems is the energy source(s) used to provide reliable and safe energy to devices within the body, which must enable systems to operate for long periods of time while minimizing the risk of infection (e.g. wires through the skin), or surgeries (e.g. to replace implanted batteries). Various avenues have been explored in recent years, such as ultrasound [12], bio-fuel cells [9], RF harvesting [30], and thermoelectric [10]. However, inductive WPT remains a safe and reliable method of providing transcutaneous energy and is particularly well suited for providing high power (10s of mW) to moderately sized implants (mm-scale) at shallow depths (sub-cm). Thus, inductive WPT is well-suited for an application such as EMG recording in the forearm as outlined in Chapter 1.

To a first order, the primary design goal for an inductive WPT link is to deliver a precise amount of energy to an implant with high efficiency. Losses include those in the circuitry itself (e.g. power amplifier switching losses, coil IR losses, and conversion losses) as well as losses in tissues and the environment around the WPT coils, as seen in the illustration in Figure 2.2. While DC-DC converters, RF-DC rectifiers, and AC power drivers can operate with efficiencies greater than 90%, the efficiency of the WPT link (η_{WPT}) can be as low as a few percent depending on the coil sizes, separation, and intervening media, and is therefore a critical parameter in the design of implantable systems.

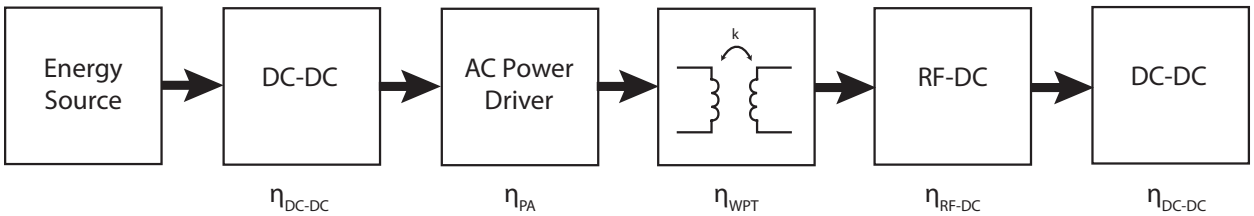

Figure 2.2: Block diagram of a typical inductive WPT for an implanted system.

2.1 Efficiency of a Two-Coil Inductive WPT Link

A two-coil inductive WPT link can be modeled with the circuit shown in Figure 2.3(a), where an AC driver (V_s) drives a resonant coil made up of resonating capacitor C_{TX}, inductive coil L_{TX}, and resistance R_{TX}. R_{TX} includes the equivalent series resistance (ESR) of the inductor and capacitor, any matching elements, and any finite source impedance, but is lumped into one parameter for ease of analysis. Energy is received by a similar circuit on the RX consisting of L_{RX}, C_{RX}, R_{RX}, and load impedance R_L. The coils are inductively coupled with coupling coefficient k representing the ratio of magnetic flux captured by the RX coil to the total magnetic flux generated by the TX coil. k is a purely geometric property of inductive links and can have values as low as 0.002 in miniaturized biomedical implant applications [31].

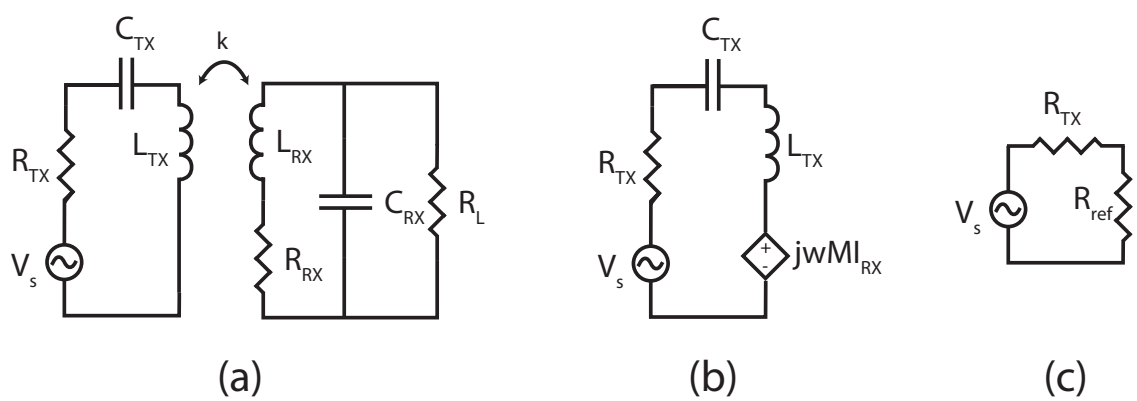

Figure 2.3: (a) Lumped circuit model of a typical two-coil inductive WPT link; (b) simplified circuit model with induced voltage from RX reflected onto TX; (c) simplified circuit model of the TX at resonance and with reflected impedance from the RX.

The effect of RX coupling can be modeled as a generated voltage (due to Faraday's Law) as shown in Figure 2.3(b), where the effect of RX coupling onto the TX is modeled by an induced voltage given by

$$V_{ref} = j\omega M I_{RX} \tag{2.3}$$

where I_{RX} is the current in the RX, j is the imaginary unit, and M is the mutual inductance given by

$$M = k\sqrt{L_{TX}L_{RX}}. \tag{2.4}$$

This induced voltage can be transformed to an equivalent reflected impedance R_{ref} as in Figure 2.3(c) where

$$R_{ref} = \frac{V_{ref}}{I_{TX}} = \frac{\omega M I_{RX}}{I_{TX}} = \frac{\omega^2 M^2}{Z_{RX}}. \tag{2.5}$$

Z_{RX} is the equivalent impedance of the secondary, which under resonance (i.e. $\omega = \frac{1}{\sqrt{L_{TX}C_{TX}}} = \frac{1}{\sqrt{L_{RX}C_{RX}}}$) is equal to

$$Z_{RX} = R_{RX} + R_{L,eq}. \tag{2.6}$$

R_{ref} models the opposing field generated by the RX according to Lenz's Law and fully determines the efficiency at the TX.

Combining eq. (2.5) and eq. (2.6) and simplifying arrives at the following expression for R_{ref}

$$R_{ref} = k^2 \omega L_{TX} Q_{RXL} \tag{2.7}$$

where Q_{RXL} is the loaded quality factor of the secondary given by

$$Q_{RXL} = \frac{Q_{RX}Q_L}{Q_{RX} + Q_L} \tag{2.8}$$

and

$$Q_L = \frac{1}{\frac{R_{RX}}{\omega L_{RX}} + \frac{\omega L_{RX}}{R_L}} \approx \omega R_L C_{RX}. \tag{2.9}$$

The last approximation holds true if $R_L >> R_{RX}$, which is usually true for biomedical implants where the equivalent load resistance is on the order of a few kΩ.

The WPT efficiency is defined as the ratio of the total amount of power that makes it to the RX load to the power generated by the TX source. The efficiency at the TX, η_{TX}, can be found through voltage division between R_{TX} and R_{ref} and is given by

$$\eta_{TX} = \frac{k^2 Q_{TX} Q_{RXL}}{1 + k^2 Q_{TX} Q_{RXL}}. \tag{2.10}$$

Similarly there is power loss in the secondary due to current division between R_{RX} and R_L which is expressed as

$$\eta_{RX} = \frac{Q_{RX}}{Q_{RX} + Q_L} \tag{2.11}$$

Combining eq. (2.10) and eq. (2.11) arrives at a total WPT efficiency

$$\eta = \eta_{TX}\eta_{RX} = \frac{k^2 Q_{TX} Q_{RXL}}{1 + k^2 Q_{TX} Q_{RXL}} \cdot \frac{Q_{RX}}{Q_{RX} + Q_L} \tag{2.12}$$

The overall efficiency is determined by the efficiency of the TX and RX, but these cannot be treated independently as R_L affects both quantities. Indeed there exists a value of R_L which maximizes the overall efficiency, as can be seen by differentiating eq. (2.12) with respect to R_L, yielding

$$Q_{L,opt} = \frac{1}{k}\sqrt{\frac{Q_{RX}}{Q_{TX}}} \tag{2.13}$$

or equivalently

$$R_{L,opt} = \frac{\omega L_{RX}}{Q_{RX}}\sqrt{1 + k^2 Q_{TX} Q_{RX}} \tag{2.14}$$

Thus there exists an optimum value of R_L which maximizes the total efficiency. R_L is determined by the power dissipation of the RX and is not available as a design parameter, but can be transformed to the required $R_{L,opt}$ through a matching network, as shown in Figure 2.4.

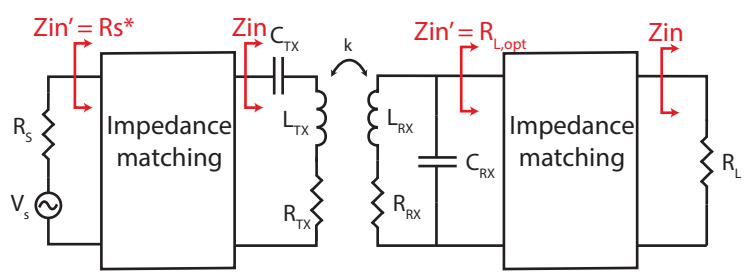

Figure 2.4: Impedance matching for maximum efficiency WPT. The RX load is transformed to an optimal load for the given set of coil parameters and coupling coefficient. The TX input impedance is transformed to the complex conjugate of the source impedance for maximum power transfer.

Finally, to determine the equivalent R_L, consider the circuit shown in Figure 2.5 which shows a typical RF-to-DC converter in a biomedical implant. Assuming that C_{rect} is sufficiently large, $V_{ac,pk} \approx V_{DC}$. To find an equivalent DC R_L, equating the AC rms power and DC power gives

$$\frac{(\frac{V_{AC,pk}}{\sqrt{2}})^2}{R_{L,AC}} = \frac{V_{DC}^2}{R_L} \Rightarrow \frac{V_{AC,pk}^2}{2R_{L,AC}} = \frac{V_{AC,pk}^2}{R_L}$$

$$\Rightarrow R_{L,AC} = \frac{R_L}{2} = \frac{V_{rect,out}^2}{2P_{RX}} \tag{2.15}$$

In order to design inductive WPT links independent of loading, an alternative metric for efficiency can be derived [32]:

$$\eta_{max} = 1 - \frac{2}{1 + \sqrt{1 + k^2 Q_{TX} Q_{RX}}}. \tag{2.16}$$

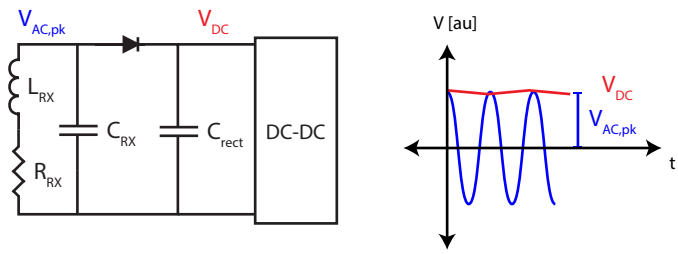

Figure 2.5: Circuit model of a typical RF-to-DC converter in a biomedical implant used to calculate an equivalent R_L.

This corresponds to the maximum achievable two-port efficiency under optimal loading, i.e.

$$Re(Z_{RX}) = R_{RX}\sqrt{1 + k^2 Q_{TX} Q_{RX}} \tag{2.17}$$

$$Im(Z_{RX}) = -X_{RX} \tag{2.18}$$

This result explains the commonly used technique of resonance at the RX, and also defines an optimal real impedance that the RX should operate with. Ignoring any losses associated with resonating out of the receiver and impedance transformation (both reasonable assumptions), eq. (2.16) provides a convenient metric for optimizing the WPT efficiency for an inductive link by allowing the designer to focus on optimizing k, Q_{TX}, and Q_{RX} without the need to design for a specific loading condition. Lastly, it is important to note that eq. (2.16) is identical to the derivation result in eq. (2.12) under optimal loading. For additional and alternative formulations of the efficiency of a two-coil inductive WPT link, see Appendix A, which includes derivations which may be useful for different simulation environments or measurement techniques.

2.2 Maximizing WPT Efficiency in Biomedical Implants

There are numerous secondary effects and losses that affect the total efficiency of a biomedical WPT link, requiring physical modeling and finite element method (FEM) simulations using tools like COMSOL or Ansys High Frequency Structure Simulator (HFSS). The following sections provide a design methodology which relies on the circuit analysis presented in the previous section, combined with circuit and FEM simulations in order to maximize efficiency in WPT links for biomedical implant applications.

As discussed earlier in this chapter, the primary design goal for an inductive WPT link for biomedical implant applications is to deliver enough energy to the implant in order for it to operate reliably. Typically, the external TX is battery powered or otherwise energy-constrained, so the efficiency of the overall WPT link is of critical importance in order to maximize the lifetime and usability of the system.

There are two main limitations on the efficiency of the WPT link: the implanted coil size and the intervening media. First, any biomedical implant should be designed to be as small as possible so that minimum tissue damage is caused during implantation and operation [33]. Thus, the size of the secondary (implanted) coil is a primary limiting factor in the overall efficiency of the WPT link and the design of this coil is of crucial importance. Second, these implants are located within lossy human tissue such as skin, fat, muscle, bone, and/or dura, affecting the electrical characteristics of the implanted coil and directly reducing the efficiency through electromagnetic (EM) power loss.

The design of the secondary coil is a critical parameter in WPT links, so it is useful to understand the physical characteristics and construction of these coils. Coils for biomedical implants are typically fabricated in one of two ways. The first and more established method consists of winding single- or multi-filament wires to create inductive coils, also known as wire-wound coils (WWC). These coils often utilize Litz wire, which is a multi-strand wire bundle designed to minimize AC resistance due to skin effect and proximity effects. It consists of multiple individually shielded thin wires bundled together in a particular weave pattern so as to equalize the portion of the total length of wire that is exposed to the surface of the wire bundle, thus minimizing losses due to the skin effect. For maximum effectiveness, each individual wire needs to have a diameter less than the skin depth of the conductor at the frequency of operation, given by

$$\delta = \sqrt{\frac{2\rho}{\omega\mu}} \tag{2.19}$$

where ρ is the resistivity, ω the frequency, and μ the permeability of the conductor. Litz wire is effective up to a frequency of about 1 MHz, corresponding to a skin depth for copper of 65 µm, since the smallest diameter wire that is readily available is around 80 µm in diameter. At frequencies above 1 MHz, the intra-wire capacitance increases dramatically and offsets the benefits of Litz wire. A few examples of commercial biomedical WWCs are shown in Figure 2.6. Multiple turns of Litz wire enable a high inductance and the Litz wire ensures a low resistance and large Q, thus maximizing efficiency. However, the frequency is limited by the use of Litz wire (usually to a few hundred kHz) and this inductive WPT setup does not scale well to small implants as will be discussed later.

An alternative implementation for implanted coils utilizes printed circuit board (PCB) technology. These printed spiral coils (PSCs) are cheaper and easier to manufacture but typically have lower Qs due to lower conductor cross-section and increased resistance. Additionally, the number of turns and fill factor (the ratio of coil outer to inner diameter) is limited due to the inherent planarity of the coils. Nonetheless, the popularity of using PSCs for implanted medical devices has increased with decreasing sizes of implants. As will be discussed in greater detail in the following section, the optimum frequency for WPT to implants increases as the implant size decreases and the implant depth increases. As implants decrease in size to a few millimeters, the optimum frequency can be hundreds of MHz or even GHz, rendering Litz wire useless. Moreover, manual construction of millimeter-sized coils is difficult and hard to control, further motivating the move towards more controlled

(a) (b)

Figure 2.6: Examples of implanted medical devices utilizing wire-wound coils (WWC) for inductive charging. Images courtesy of Nevro and Advanced Bionics [34, 35].

and accurate PCB technology for coil construction.

The result in eq. (2.16) suggests that maximizing the efficiency of an inductive WPT link can be achieved by maximizing k, Q_{TX}, and Q_{RX} independently of each other. However, the effects of lossy tissue on the link itself, and in particular on Q_{TX} and Q_{RX} is not considered. The presence of lossy media between or near the inductive WPT coils affects the maximum achievable efficiency in two main ways: tissue losses and coil detuning. The former is usually assumed to have a negligible effect when the operating frequency is in the kHz or low MHz range, as is the case for the majority of traditional implanted links. However, as the size of the implanted coil decreases, the optimum frequency for WPT increases and significant tissue interaction occurs [28]. Thus, it is critical to fully model the inductive WPT link and its surrounding media in order to design a link that operates with maximum efficiency. The simulation environment Ansys HFSS is utilized to fully model the inductive WPT links throughout this thesis.

The second efficiency loss factor is due to a decrease in implanted coil Q arising from increased coil-tissue interaction. Implanting a coil inside a lossy medium increases the parasitic capacitance of the coil and decreases its self resonant frequency (SRF). As a result, the Q and efficiency decreases significantly unless designed specifically for the environment in which it is implanted. This effect is particularly pronounced for implanted coils with large numbers of turns. Figure 2.7 shows HFSS simulation results of implanted coil Q as a function of frequency for various coils in air and implanted under 2mm of skin and 2mm of fat, with 10mm of muscle underneath, for example for an EMG application. The coils are square and constrained in area to $25\,\mathrm{mm}^2$ with a 3 mil trace width and spacing in order to limit the design space. The trace material is copper with a thickness of 1.4 mil. When a coil is operated in air (or is not near lossy media), Q is maximized when the number of turns is large. However, when coils are placed next to or within lossy media (such as skin, fat, and muscle), Q is maximized for small numbers of turns (in most cases a single turn) since the increased trace area of coils with large N increases the parasitic capacitive coupling to the surrounding tissue. It is worth noting that the trends present in these simulations hold true independent of trace width and spacing.

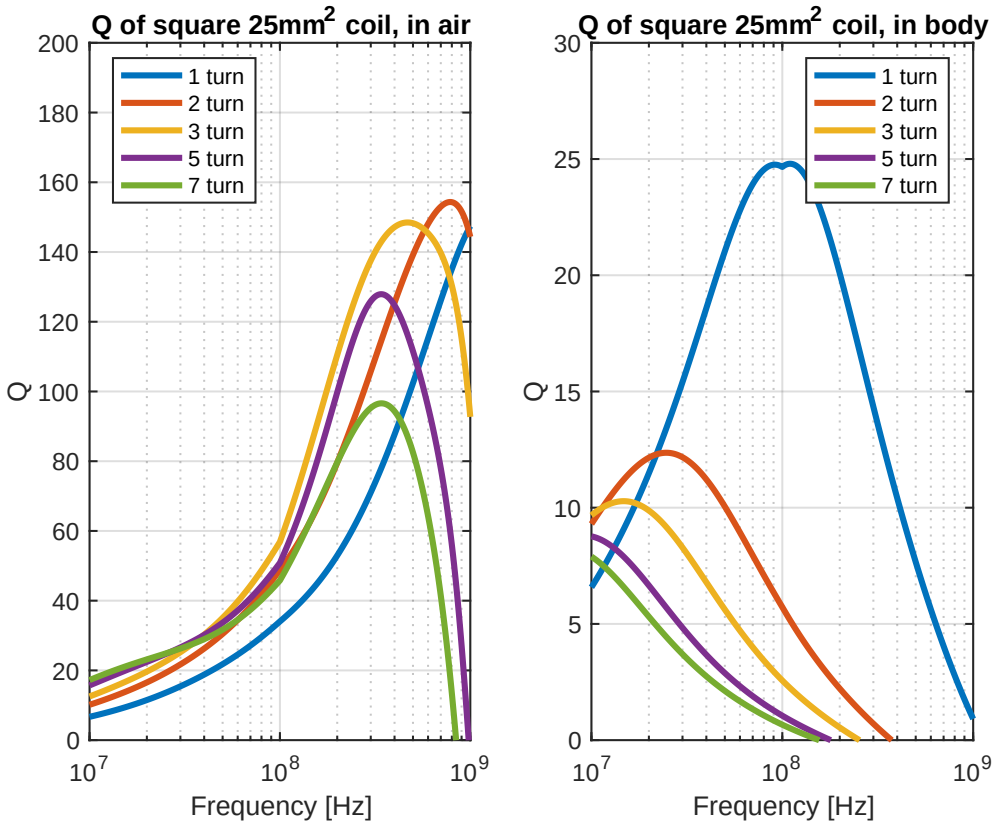

Figure 2.7: Coil quality factor (Q) as a function of frequency for different number of turns in air (left) and body (right). The increase in parasitic capacitance due to tissue interaction decreases the SRF of the implanted coil and leads to a maximum Q achieved with a single turn coil.

2.3 Design Methodology for Maximum Efficiency Two-coil Inductive Links

A number of optimal design methodologies for designing high efficiency inductive WPT links exist [31, 36]. These methodologies, however, rarely include all pertinent parameters in order to constrain the design problem to a manageable scope. Indeed, it is extremely difficult to fully model the entire WPT link in terms of magnetics, secondary losses, coil interactions, etc., so it is prudent to limit the design space according to the particular application. Therefore, this thesis proposes a design methodology specifically aimed at the application of chronic EMG recording at the forearm as outlined in Chapter 1. More specifically, the goal is to design a high efficiency WPT link that is able to energize multiple, randomly distributed implants within a certain area. The design of this single-input multiple-output (SIMO) link

begins by optimizing a single TX coil to optimally power a single implant in this chapter, and then extends this to an array of coils designed to power a large area in Chapter 3.

This section outlines the methodology and reinforces it with a design example and HFSS simulation results. It considers all relevant constraints and important design parameters with the goal of designing a maximally efficient inductive WPT link. As discussed in the previous section, the efficiency of an inductive WPT link is a complex function of coil geometry and channel, and thus a closed-form solution is difficult to ascertain. The design of an inductive WPT link for an implant can be simplified and codified as shown in the diagram in Figure 2.8 by considering the various requirements, constraints, and tradeoffs discussed in this section. The design methodology relies on the fact that TX and RX coils can be optimized somewhat independently while achieving good results, as suggested by [31, 36]. Nevertheless, the process outlined can be extended to an iterative one in order to more fully model inter-coil interactions and consider all potential loss sources.

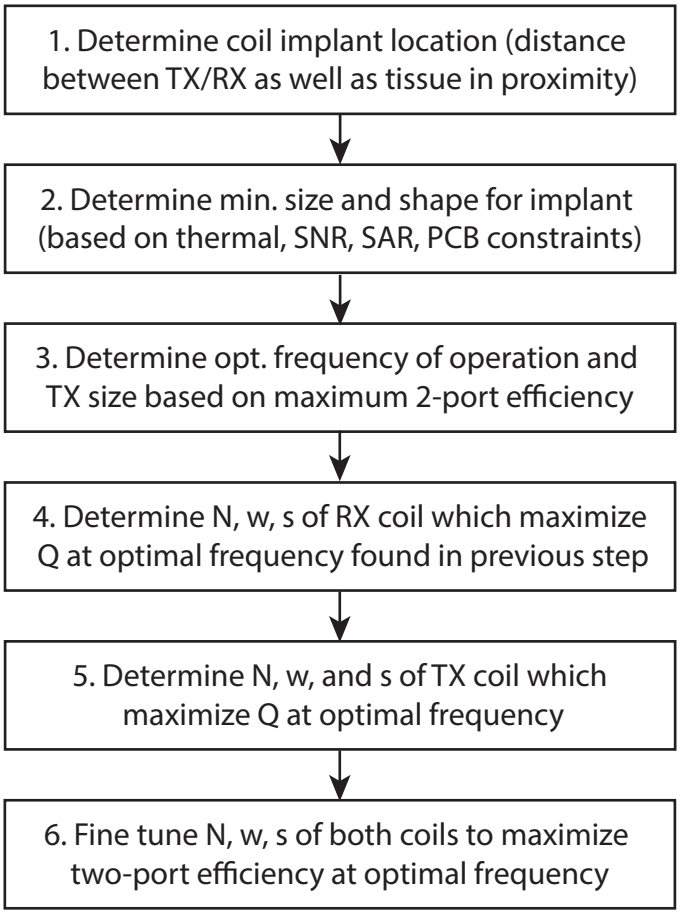

Figure 2.8: Flow chart for design of maximum efficiency two-coil inductive WPT links for implanted medical devices.

Step 1: Determine implant location
The application explored in this work aims at recording EMG signals from the muscles of the forearm. The implant is located under 1mm air, 2mm skin, and 2mm fat, chosen as average thicknesses in an adult forearm [37, 38], with 10mm of muscle underneath.

Step 2: Determine implant size and shape
Since most parameters relevant to inductive WPT are directly dependent on coil size, this step is the most important in determining the maximum achievable efficiency. For this EMG recording implant, the minimum size is approximately 36 mm^2 (for details on the derivation of this, refer to the discussion in Chapter 4). It is assumed that the RX coil is wrapped around the electronics in order to minimize total implant size, so its maximum area is also 36 mm^2. With the size and location of the implant determined, the shape of the implant can be decided. Figure 2.9 shows HFSS simulation results for the maximum achievable efficiency from eq. (2.16) for a 36 mm^2 rectangular implanted coil as a function of the aspect ratio (ratio of width to length). In each case, both the RX and TX coils are constructed with the same aspect ratio in order to match the magnetic field distribution. As can be seen, while a large aspect ratio may improve the "implantability," for example by allowing for injection using a hypodermic needle as in [39], the efficiency is maximized when using a square coil. Thus, a 6 mm by 6 mm coil is assumed throughout the rest of this section.

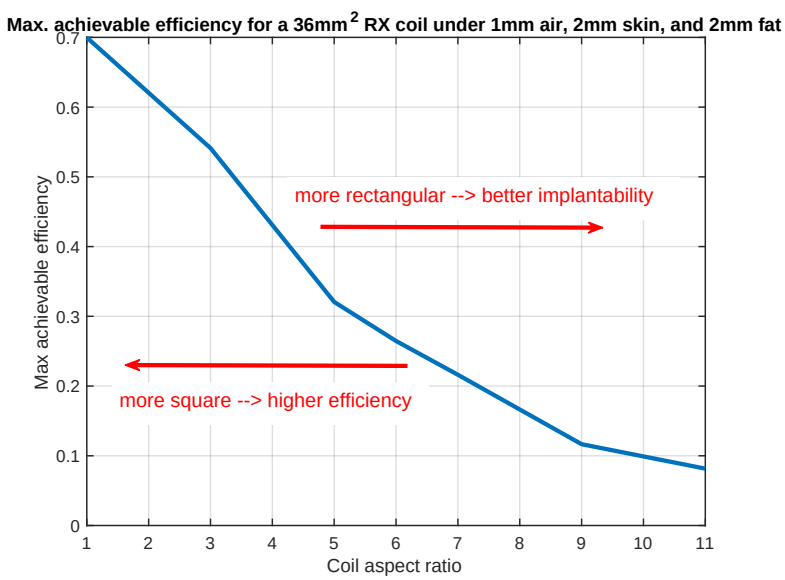

Figure 2.9: Maximum achievable WPT efficiency to a 36 mm^2 implanted coil under 1mm air, 2mm skin, and 2mm fat.

Step 3: Determine optimal TX size and frequency
Once the RX coil size, shape, and location are determined, the next step is to choose a TX size and frequency which maximize the efficiency to that particular implant geometry. It has been shown that there exists an optimum TX size and frequency pair for any specific

implant geometry [40, 41, 42]. In order to determine this optimum TX size - frequency pair, HFSS simulations were performed using the channel model and tissue parameters shown in Figure 2.10 and Figure 2.11. The channel consists of 1mm air, 2mm skin, and 2mm fat, with 10mm of muscle underneath. Tissue parameters are extracted from [43] for the frequencies of interest (10 MHz to 100 GHz). The results of these simulations are shown in Figure 2.12 for a 6 mm by 6 mm coil powered by TX coils of different sizes. The TX coil geometry is a single-turn hexagonal loop chosen to maximize homogeneity when tessellated, as will be discussed in Chapter 3. These results suggest that the optimum TX coil has a 12mm diameter and operates at 160 MHz. Furthermore, the maximum efficiency is not very sensitive to the exact size of the TX as long as the frequency is correctly chosen for each given TX size.

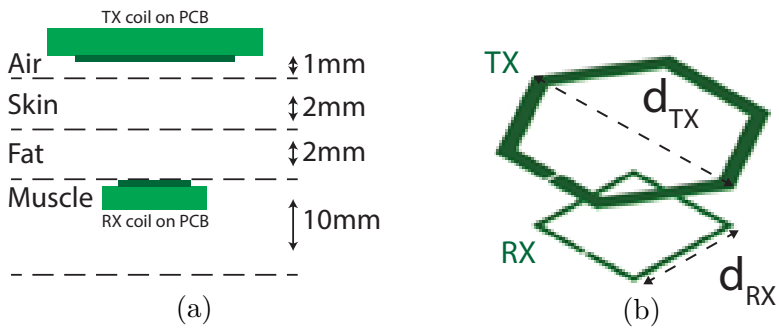

Figure 2.10: (a) Channel and (b) coil geometry used in HFSS simulations. PCB and tissue media are not shown in (b) for clarity.

Step 4: Determine RX coil geometry

Next, the specific geometry of the RX can be determined based on HFSS simulations. As discussed in the previous section, when a planar coil is implanted in lossy media, its Q is maximized for a design with few turns. Thus, the implanted coil is chosen to have a single turn and the only design parameter that needs to be determined is its trace width, w. A wider trace width reduces the parasitic resistance and increases Q, but decreases the available area inside the coil for components and routing in the full system. Thus, there exists a tradeoff between Q (and efficiency) and the area required for circuit components. Figure 2.13 shows simulation results for Q for different trace widths at the optimal frequency of 160 MHz. The final trace width chosen is 6 mil (152.4 µm) as this achieves a moderate Q of 35 while allowing for the majority of the 36 mm^2 PCB area to be used for components and routing.

Step 5: Determine TX coil geometry

Similar to the RX optimization, the TX coil's number of turns, trace width, and trace spacing are optimized for maximum Q at the operating frequency. As will be explained in the following chapter, the TX is hexagonal in shape. The frequency and TX diameter are fixed from Step 3 to 160 MHz and 12mm, respectively. HFSS simulations were performed

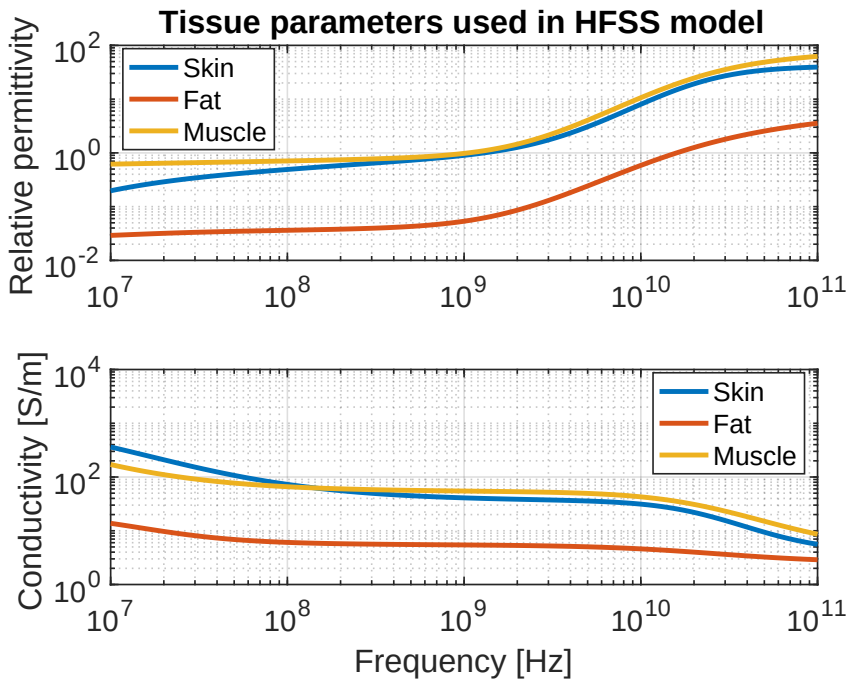

Figure 2.11: Tissue properties used in HFSS simulations.

for different TX coil geometries by sweeping N, w, and s and calculating the efficiency to the RX. These simulations show that larger number of turns achieves higher efficiencies since Q tends to increase with more turns. However, the final goal of this WPT link is to power a large area by tessellating the individually optimized TX coil, so another important metric is the magnetic field homogeneity of the tessellated array. Figure 2.14 shows the efficiency and homogeneity of the TX with variable number of turns. It is evident that although the maximum efficiency increases with a greater number of turns, the homogeneity of the field decreases significantly, and therefore a single turn coil is best for this application.

Step 6: Fine tune coil parameters

As an optional final step, the full two-coil link is simulated using the setup shown in Figure 2.10. Coil parameters and frequency are swept around the design point to find the final optimum parameters, which are shown in Table 2.1. The final efficiency as a function of frequency is shown in Figure 2.15. The maximum efficiency of 69.51% is achieved at the optimum frequency of 160 MHz, but there is a relatively flat peak, suggesting that frequency deviation due to resonance shifts post-implantation would not have an adverse effect on the overall link efficiency.

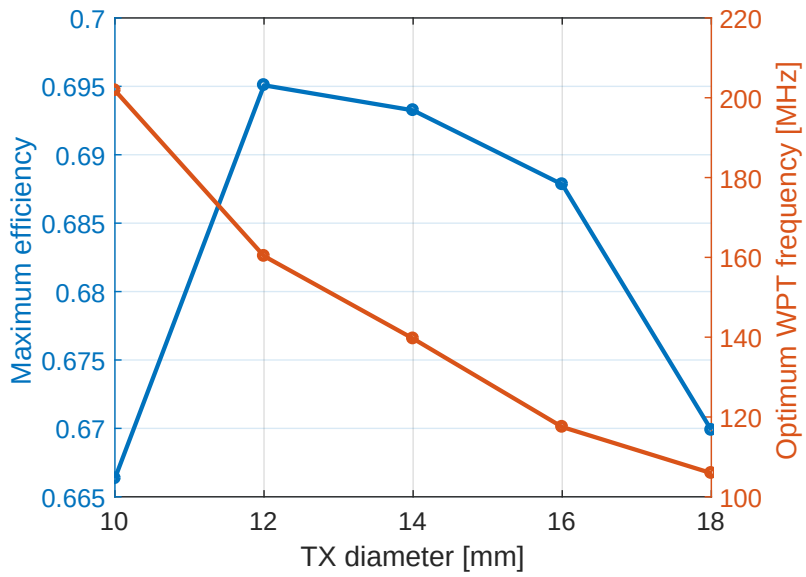

Figure 2.12: Maximum achievable efficiency and optimum WPT frequency as a function of TX diameter. This plot shows that the maximum achievable efficiency for WPT to a 6 mm by 6 mm implant is achieved by using a 12 mm diameter TX at a frequency of 160 MHz.

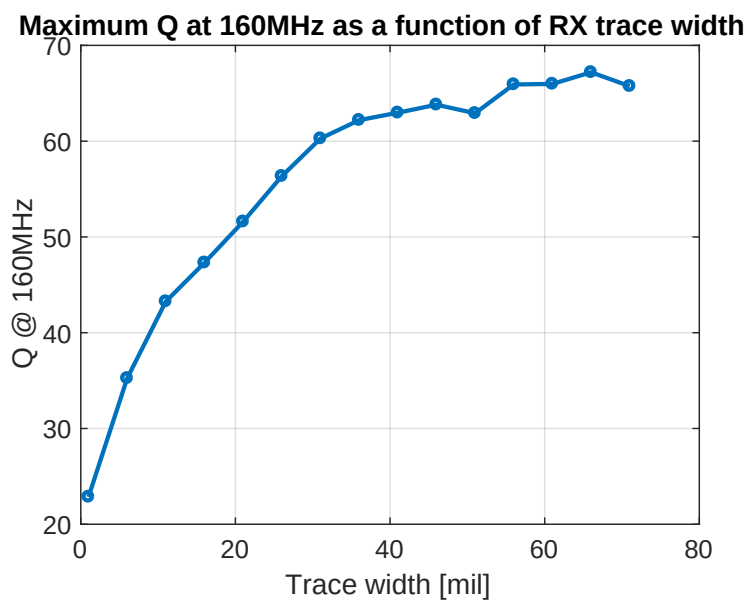

Figure 2.13: Q at 160 MHz for different RX trace widths.

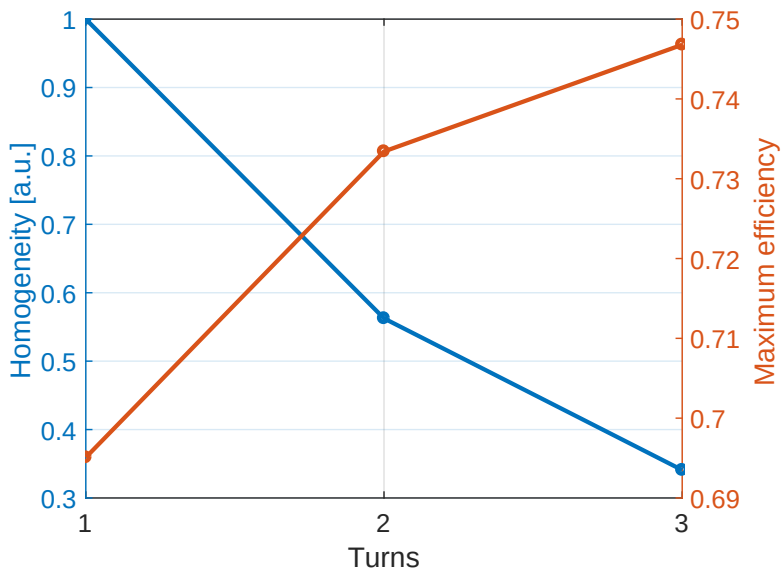

Figure 2.14: Efficiency and field homogeneity for a 12mm hexagonal coil with varying number of turns.

Table 2.1: Coil geometry for optimal WPT to an implant in the forearm

	TX coil	**RX coil**
Shape	Hexagonal	Square
Outer diameter (d_o) [mm]	12	6
Trace width [mm]	0.762	0.1524
Turns	1	1
Substrate	FR-4 PCB	
Frequency [MHz]	160	
Media between coils	1mm air, 2mm skin, 2mm fat	
Media underneath implanted coil	10mm muscle	
Maximum efficiency (simulated)	69.51%	

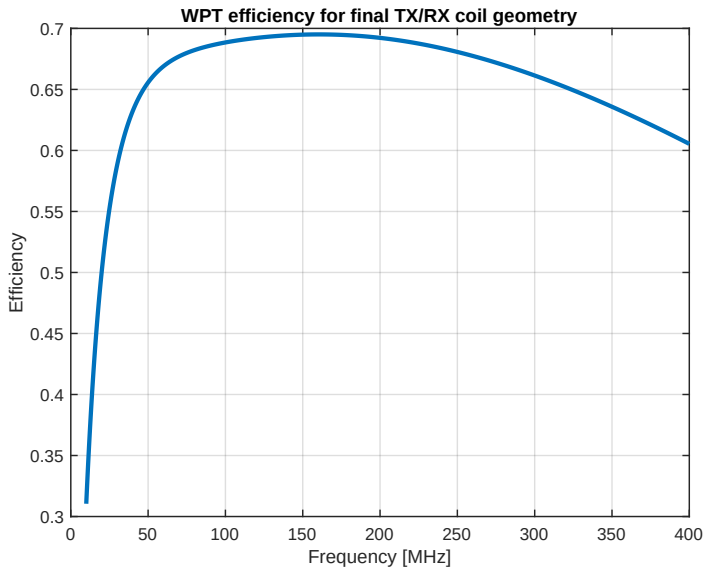

Figure 2.15: Final WPT efficiency for coil geometry from Table 2.1. The maximum efficiency of 69.51% is achieved at the optimum frequency of 160 MHz.

2.4 Summary

This chapter detailed the use of inductively coupled wireless power transfer links for powering implanted biomedical implants with an emphasis on high efficiency operation. The physical origin of the power transfer was described and used to define various system parameters which can improve the power transfer capabilities of an inductive WPT link. Various other system-level considerations were presented that motivate design decisions. The overall efficiency of a WPT link was shown, with particular emphasis on the efficiency of the two-coil inductive link. A simplified circuit model for an inductive link was presented and the two-coil efficiency derived, as well as a simplified metric for maximum achievable efficiency under resonance and optimal loading.

These theoretical and mathematical results were used to motivate various design decisions for maximizing the efficiency of an inductive WPT link in biological media. Ansys HFSS simulations were used to validate assumptions and demonstrate tradeoffs. A design methodology for designing maximum efficiency inductive WPT links for biomedical implants was presented, along with a guiding example for a system which records EMG from multiple locations on the forearm.

Chapter 3

Inductive Wireless Power Transfer to Multiple Biomedical Implants

As electronics and packaging technologies advance and the size of implants shrinks, implanting multiple devices inside the body becomes a real possibility. The Human Intranet introduced in Chapter 1 envisions a scenario in which multiple small EMG-recoding nodes are implanted in the forearm to record EMG signals for the purpose of controlling a prosthetic. It is not unreasonable for the size of these implants to approach mm-scale, or even smaller. In this scenario, the distance between any pair of implants is large relative to the size of the implants, for example on the order of centimeters. Providing energy to a set of randomly distributed implants such as in this prosthetic application is exceedingly challenging using traditional inductive WPT approaches. In traditional inductive WPT, each implant is powered by a dedicated external coil which requires precise alignment and power control. While this scheme works for a small number of implants, as the numbers of implants scales so does the complexity of providing power. How do you ensure coil alignment among multiple implants and external coils? Does each external coil include a dedicated energy source and control circuitry? And perhaps most importantly, how do you deliver precise and efficient wireless power if the locations of the implants are random or even time-variant?

Multiple works have investigated inductive WPT for multiple receivers [44, 45, 46, 47], spanning a wide breadth of applications, power levels, and coil sizes. In [44] the authors utilize a four-coil WPT link consisting of large diameter (30 cm) TX coils powering multiple small (1.3 cm) coplanar RXs. In [45] the authors propose an impedance matching technique to provide adjustable power to multiple RXs with different coupling. In [46] the authors present an inductive link for WPT to mm-sized neural implants which utilizes a high-Q implanted resonator coil encompassing the implants. The link operates at 60MHz and achieves a power delivery and efficiency of 1.3 mW and 2.4%, respectively, but has a limited spatial coverage and the implants must reside in a $7\,\mathrm{cm}^2$ area. [47] proposes a platform for powering multiple mm-sized neural implants by using tessellations of coils to generate a homogeneous magnetic field at the location of the implants. However, measurement results are shown on a scaled-up prototype for powering an implant on a freely behaving animal in a cage

environment and no validation in body or for multiple RXs is performed.

To the author's knowledge, no work exists which explores the optimal method of inductively powering multiple mm-scale biomedical implants distributed across a large area of the body. Prior work in [46, 48] has shown promising results for powering multiple neural implants but both have small areas of coverage. A system that allows for such a powering scheme must be modular, simple, highly efficient, and provide reliable power to multiple locations. Modularity would enable the powering scheme to be used in different locations around the body and allow for the same system to be used for applications with large and small coverage (e.g. distributed EMG and localized neural sensing, respectively). Additionally, low complexity encourages widespread adoption while limiting the energy and computational overhead on existing systems. Combined with a high overall system efficiency, such a powering scheme would extend the operational lifetime of the implanted system and enable chronic use.

In this chapter, one solution for powering multiple randomly distributed biomedical implants is presented. The application of distributed implanted EMG recording outlined in Chapter 1 is used as a guiding example, allowing to compare various powering strategies directly to each other under a common set of design constraints.

3.1 Hexagonal Tessellations for Homogeneous Inductive Wireless Power Transfer

The main goal of a multi-receiver WPT link design is to provide uniform power to multiple distributed implants with maximum efficiency. Traditional wireless power transfer for medical implants relies on precise alignment between an external coil and the implant to guarantee efficient and reliable power transfer, e.g. in [6, 25]. In a distributed system, wireless power needs to be generated across a large area covering multiple implants [12, 46]. In other words, both the efficiency to a single implant and the homogeneity across a given area must be maximized, so it is useful to define quantitative metrics for these properties.

Throughout the rest of this thesis and without a loss of generality, the maximum power transfer efficiency of a multi-coil WPT link η_{max} is defined as:

$$\eta_{max} = 1 - \frac{2}{1 + \sqrt{1 + \chi}} \tag{3.1}$$

where χ is the sum of squares of kQ-products of each pair of coils in the system. For a traditional two-coil link, χ is simply the product of the coupling factor k^2 and the individual unloaded quality factors of TX and RX coils, Q_1 and Q_2, respectively, as derived in Chapter 2. For a system with multiple transmitters (MISO), multiple receivers (SIMO), or both (MIMO), χ is given by [32]:

$$\chi = \sum_{i=1}^{N} \sum_{j=1}^{M} k_{i,j}^2 Q_i Q_j \tag{3.2}$$

where N and M are the number of transmitters and receivers, respectively.

The uniformity of the power distribution scheme is characterized using the coefficient of variation (CV) of the magnetic field,

$$CV = \frac{\sigma_{H-field}}{\mu_{H-field}} \tag{3.3}$$

where σ and μ are the standard deviation and mean of the magnetic field strength, respectively. CV is calculated across a plane parallel to the surface of the transmitting coil, with a low value of CV corresponding to good homogeneity. CV provides a reasonable first-order evaluation of the magnetic field homogeneity and is scale invariant, so the results are independent of the applied power at the TX.

The previous chapter discusses the requirements and design methodology for maximum efficiency inductive WPT links for traditional two-coil links. The ideas and analyses presented therein can also be applied to the design of wireless power links for multiple implants. One of the simplest methods of providing wireless power across a large area is to utilize a large TX coil which encompasses multiple RX, for example as in [44, 46]. An example is illustrated in Figure 3.1 for an EMG application, showing a single large coil covering an approximately 20 cm^2 area encompassing three implants. The link can be modeled as a set of traditional two-coil links with coupling coefficients k_i, as shown in Figure 3.1(a). These coupling coefficients are approximately equal to each other as all RX coils are assumed to be the same size and at the same vertical distance from the TX coil, and the magnetic field strength inside the TX coil can be treated as uniform for a coil with a large number of turns. Note that any coupling among RXs is assumed negligible, which is a reasonable approximation if the distance between any two RX is larger than the size of an individual RX.

As shown in Chapter 2, the optimum TX size to power a 6 mm by 6 mm implant under 1mm air, 2mm skin, and 2mm fat is 12mm. Using a coil larger than this results in lower efficiency WPT due to a smaller coupling coefficient (less of the generated magnetic flux couples to the RX coil) and more losses in the primary. As a result, the efficiency to a single implanted node is much lower than in the ideal, optimized two-coil case. To explore this further, HFSS simulations were performed in which a single RX coil was swept within the 48mm by 40mm area and the two-coil maximum achievable efficiency given in eq. (2.16) was calculated at each location. The results of this are shown in Figure 3.2, where the large TX efficiency is plotted in blue. The shaded region represents the deviation of the efficiency as the RX is moved around within the area, while the solid line represents the average efficiency. The efficiency is maximized when the RX coil is centered on-axis with the TX and the minimum efficiency is achieved when the coil is closest to the edge of the TX coil, as expected. The maximum average efficiency is only 39.7% compared to the ideal case of 69.5%, plotted in red for reference. More importantly, the efficiency of the large coil design decreases as the coverage area increases, as the TX coil size further deviates from the optimum and k is reduced. Therefore, this is not a scalable technique for powering implants distributed over a large area.

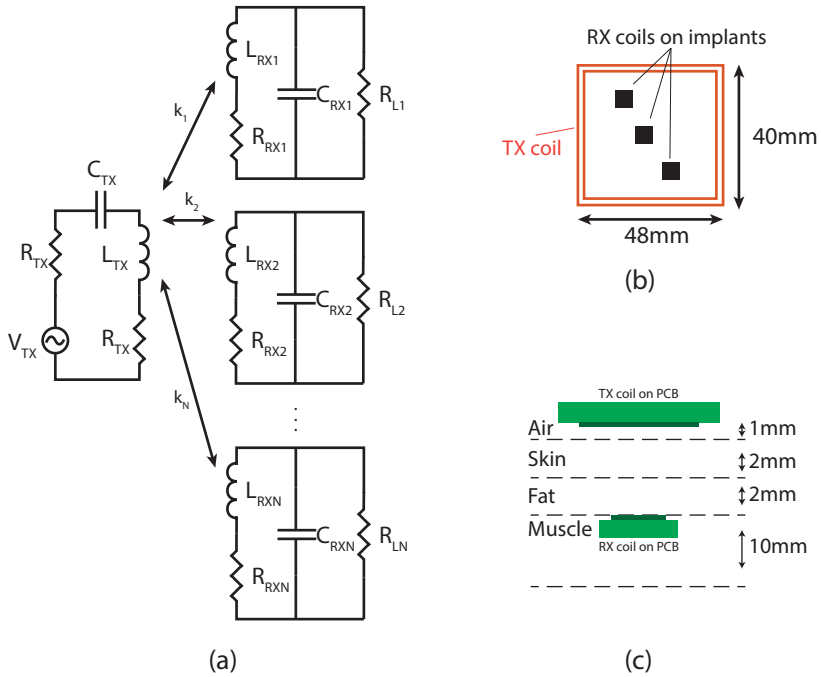

Figure 3.1: (a) Circuit model of an inductive WPT link with a single TX and multiple RX coils; (b) illustration of a 48mm by 40mm coil powering 3 randomly located 6 mm by 6 mm nodes (not to scale); (c) cross section of the implant location relative to the external large TX.

Another method of powering a large area is to tessellate multiple smaller coils into a two-dimensional (2D) grid and adaptively select which subset of coils to power, as first proposed for position-agnostic inductive charging of consumer electronics [49]. This technique increases the complexity of routing and driving architecture but can achieve a much higher average efficiency and homogeneity. Figure 3.3(a) illustrates how hexagonal coils can be arranged to generate a homogeneous magnetic field over a large area. The magnetic field generated by a single coil has a maximum at the center of the coil and decreases away from this point, resulting in minima (-) and maxima (+) when the coil is tessellated to create a magnetic "surface" as shown in Figure 3.3(b). To improve the homogeneity, six equivalent coils are added in two layers such that their maxima coincide with the minima of the original coil to create a building block which is used to cover a large area. Any implant located underneath the array is guaranteed to be closely aligned to the center of at least one TX sub-coil and see a similar magnetic field and coupling. This improves the CV of the array by 32.7% when compared to a single layer approach. Note that, while any coil shape that tessellates can be arrayed in this way, a hexagonal tessellation achieves complete minima/maxima cancellation with the fewest number of layers (three compared to four for rectangular coils).

The maximum efficiency of such an array is still determined by eq. (3.1), with χ defined as

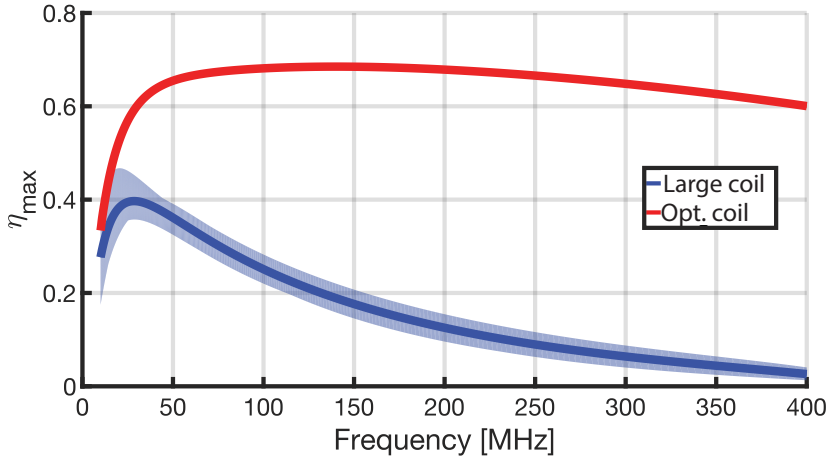

Figure 3.2: Efficiency as a function of frequency for a single 48mm by 40mm TX coil powering a single implant located in a random position within the coil area, in blue. The efficiency of an optimized TX coil, as designed in Chapter 2, is also shown for comparison, in red.

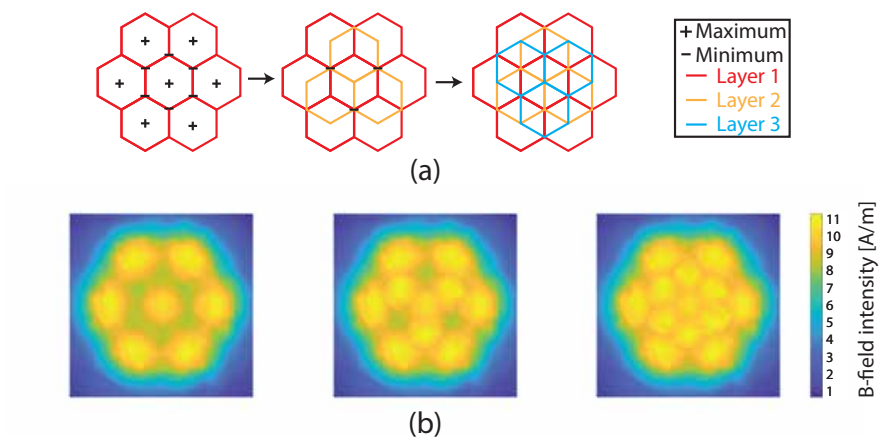

Figure 3.3: (a) Concept of a three-layer coil structure designed to generate a homogeneous magnetic field for WPT to multiple implants; (b) magnetic field strength for the three coil structures in (a).

the sum of squares from each TX array sub-coil to a single implant. Achieving this maximum efficiency requires both RX load tuning given by:

$$\mathrm{Re}(Z_{RX}) = R_{RX}\sqrt{1+\chi} \tag{3.4}$$

$$\mathrm{Im}(Z_{RX}) = -X_{RX} \tag{3.5}$$

and TX currents satisfying the following:

$$I_1 : I_2 : ... : I_N = \frac{X_{1,N+1}}{R_1} : \frac{X_{2,N+1}}{R_2} : ... : \frac{X_{N,N+1}}{R_N}. \tag{3.6}$$

While the first condition is easily achieved with standard resonance and impedance matching, the second is difficult to implement without significant power and complexity overhead. This second condition requires that each sub-coil in the array be driven with a current proportional to its coupling to the receiver. This can be implemented by monitoring the impedance of each sub-coil and using the reflected impedance to calculate the coupling, but the complexity of such an approach is not suitable for a low-power and scalable array architecture. Furthermore, each sub-coil requires a dedicated power amplifier (PA) and control circuitry, further complicating routing and decreasing the Q of the TX array and the efficiency of the overall link.

The efficiency of an independently-driven array is characterized when powering randomly distributed implants and compared to the case of a single large coil covering the same area, as illustrated in Fig 3.4. A 48-coil array made up of three layers of 16 coils each is constructed in HFSS with an independent port driving each coil. The three layers are driven using time division multiplexing (TDM) such that only one layer is driven at any time. A single RX is located in a random location within a 40mm by 48mm rectangular area 5 mm below the array, chosen such that no edge effects are seen due to the finite size of the array. The location of the RX is swept across this region in steps of 3 mm and the efficiency given by eq. (3.1) is calculated at each position. Figure 3.4(b) shows the efficiency above of this array as well as above an equivalent area single coil, as a function of the position of an RX above. While the large coil achieves a maximum efficiency around 55%, the efficiency significantly decreases as the position of the RX moves away from the optimum center and towards the edges of the coil, eventually reaching zero when the RX coil bisects an edge of the TX coil and the total magnetic flux is 0. On the other hand, the array achieves a higher maximum efficiency of 70.3%. More importantly, the homogeneity of the array is greatly improved and the mean efficiency is 68.5%, since the RX is guaranteed to be close to the center of at least one TX sub-coil. Finally, Figure 3.4(c) shows the two TX coils powering three randomly located RX simultaneously. Large variations in efficiency are clearly seen with the single large coil, which achieves maximum efficiencies of 57.5%, 40.4%, and 3.96% for each of the RX. On the other hand, the array achieves efficiencies of 67.5%, 68.3%, and 67.0%, demonstrating the ability to power multiple implants simultaneously.

The fact that the maximum efficiency from the 48-coil array is the same as a standard two-coil link in Chapter 2 is not a coincidence. Indeed, eq. (3.6) suggests that most of the current in the TX array is located at the sub-coil with largest coupling to the RX. As a result, the array can be approximated as a single sub-coil coupled to the implant. In the case of multiple implants as in Figure 3.4(c), it is equivalent to multiple single-coil links operating in parallel, each with an efficiency around the maximum found in Chapter 2 (70%). These results ignore any overhead power and losses from driving the array. A real implementation would require dynamic updating of TX currents, especially if the TX and/or RXs move with respect to one another, and the computation required would reduce the overall efficiency. More importantly, the overhead computation and power would scale linearly with the size of the coverage area and is not ideal for an energy constrained system such as chronic EMG.

3.2 Single Driver Hexagonal Array

One possible solution to the problem of increased complexity is to drive the TX array with a single PA, eliminating the need for complex routing, TX calibration, and dynamic load tracking. A variety of driving architectures were explored for a single layer array and are illustrated in Figure 3.5, namely independent, parallel, series, and series-parallel. Driving each coil independently produces the highest homogeneity (lowest CV) as seen in the right of the figure, assuming the PAs are located directly underneath the array and therefore do not require long routing traces. Driving the array in parallel increases the SRF but exhibits the highest CV due to current division caused by long traces. Alternatively, driving the array in series ensures that all coils are driven with the same current and therefore produce the same magnetic field, but SRF is decreased and the inter-coil routing is more complex which disturbs the magnetic field. A combination of parallel and series connections demonstrates the lowest CV and allows control over the SRF of the array through varying the number of rows and columns driven. In this method, each row is connected in series and these rows are driven in parallel by a PA located on the edge of the array. The routing layer (shown in blue) is less complex and minimizes the magnetic field perturbations, allowing for good homogeneity.

The efficiency of the single-driver array can again be calculated from eq. (3.1), in this case for a SISO link (for an array powering a single implant). Due to the decreased SRF and Q of the TX array, the new maximum efficiency is 8.19%. However, this efficiency increases with an increasing number of RX. In this case, the link is SIMO and χ is the sum of kQ products from the array to each individual RX. Since all $k_{1,i}$ are equal by design (equal coupling between TX and any RX), maximizing the total efficiency is achieved by maximizing each individual Q independently. An important result of this is that the total system efficiency can be increased by adding more receivers, and asymptotically approaches that of a MIMO array as can be seen in Figure 3.6. The effects of cross-coupling can be mitigated by correctly selecting the reactance of the RX loads (see equations 34-35 in [32]).

The three layer version can also be driven with a single PA. A 3:1 RF multiplexer switch selects among the three layers in a time-division multiplexing (TDM) fashion. The TDM switching period is determined based on the WPT frequency, time constant of the RX rectifier, and any requirements on RX supply ripple. The un-selected layer is left open such that no magnetic coupling occurs, since any induced current cannot flow around the individual sub-coils.

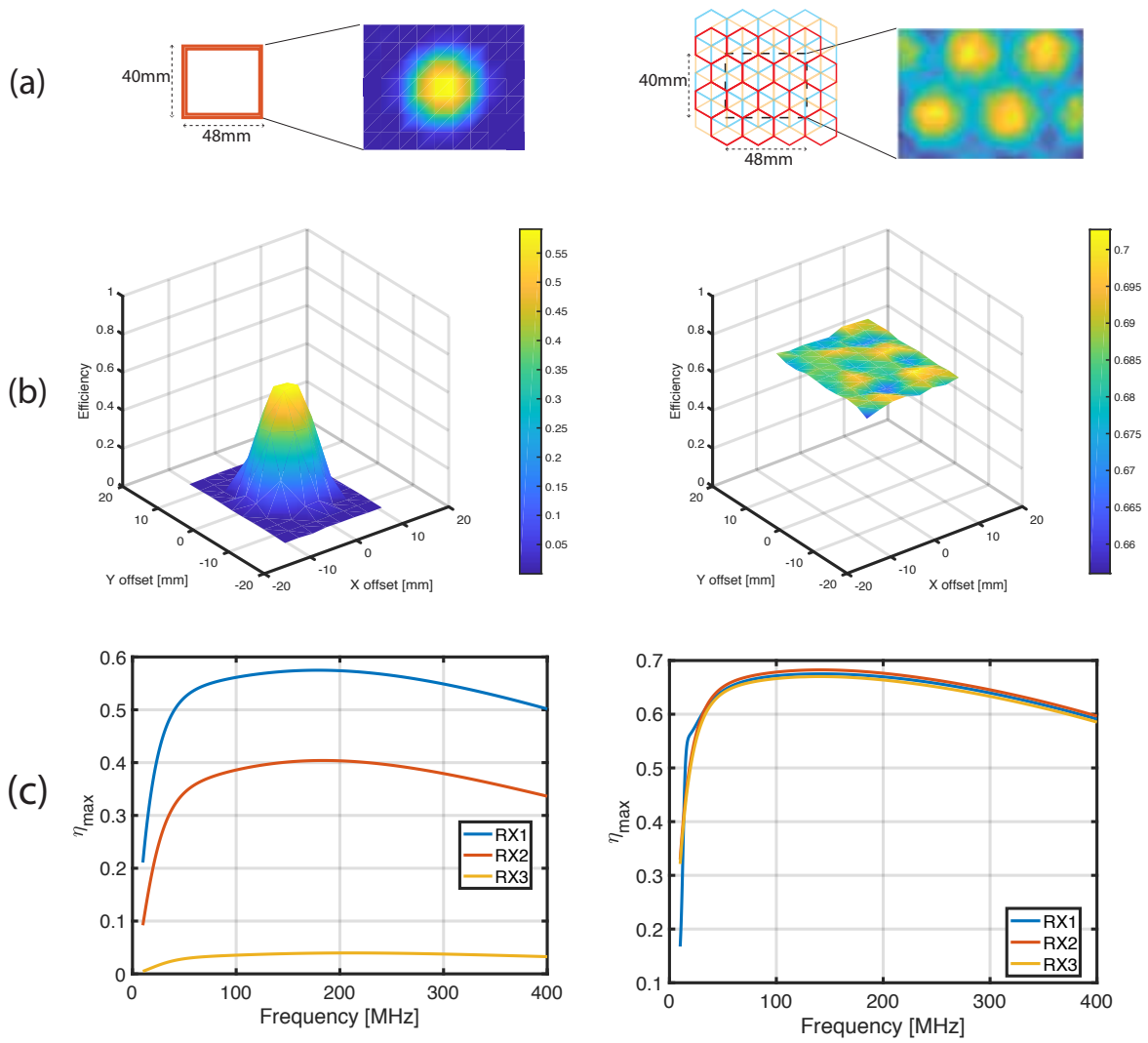

Figure 3.4: (a) A large single coil (left) and a 48-coil array (right) constructed in HFSS and their corresponding magnetic field distributions. Only a single layer made up of 16 coils is driven in this simulation. (b) Maximum efficiency distribution of the single coil (left) and array (right) powering a single randomly located RX swept across the rectangular area outlined in (a). (c) Efficiency of simultaneous WPT to three distinct RX positioned randomly underneath the large coil (left) and array (right).

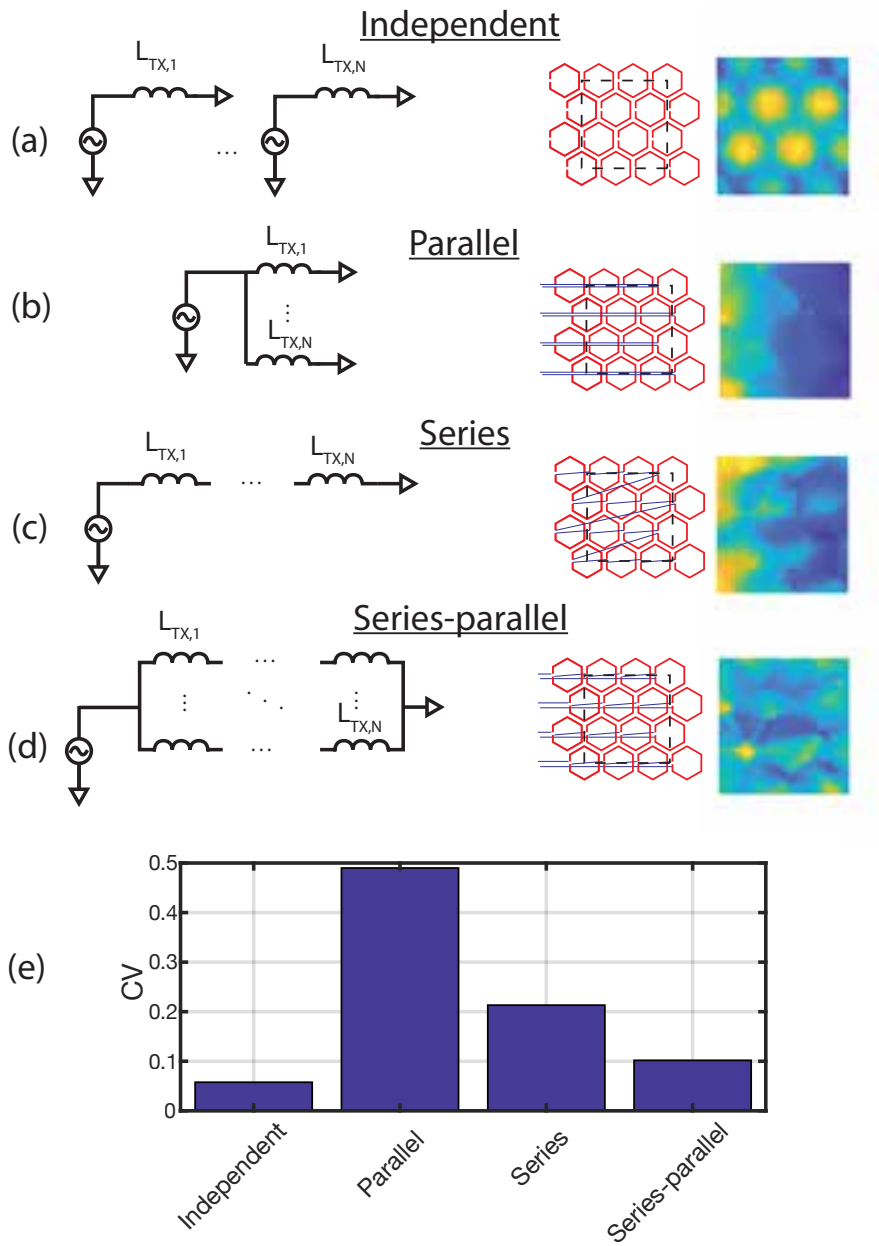

Figure 3.5: (a) Independent, (b) parallel, (c) series, and (d) series-parallel topologies for a multi-coil single layer array. Schematic diagrams show driving architecture (left). Layout illustrations (center) show two distinct routing layers for coils (red) and interconnects (blue). The magnetic field strength plots (right) show the magnetic field variations within a rectangular area above the array, chosen such that no edge effects are captured due to the finite size of the array. (e) Coefficient of variation (CV) for the four driving topologies.

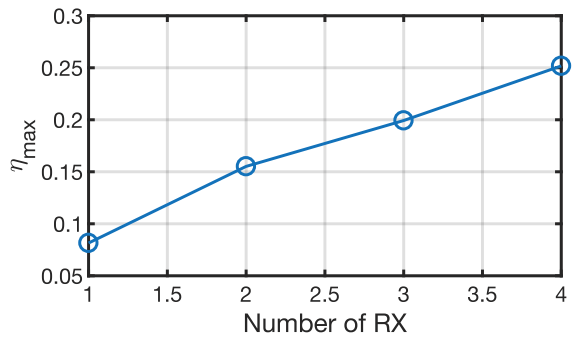

Figure 3.6: System efficiency of a series-parallel driven array as a function of the number of RX.

3.3 Summary

A novel coil structure for powering distributed implants was presented which utilizes a TX coil optimized for maximum WPT efficiency to a single implant. This sub-coil is tessellated to form a 2D array in order to cover a large area and provide equal power to any implant located beneath it. Two more layers may be added in an offset manner in order to improve the homogeneity of the array by minimizing the magnetic field strength variations at the edges and corners of individual sub-coils. Various methods of driving this array are proposed and tradeoffs discussed with a mobile, energy constrained application in mind. It is shown that while an independently driven array (in which each coil is driven by a dedicated PA) provides the highest efficiency and best homogeneity, it is too complex for a wearable, low-power platform required for chronic EMG. A technique for combining sub-coils is proposed which achieves reasonable homogeneity, but with a reduced efficiency. However, this approach is flexible and allows for different sized arrays to be driven in a similar fashion, enabling user customization. Last, it is shown that the total system efficiency of this array can approach that of an independently driven array as more implants are added to the system, although this is application specific.

Chapter 4

EMGnode - A System of Distributed EMG-recording Implants

4.1 Introduction

Electromyography (EMG), the recording of the electrical activity of muscles, is an easily accessible physiological signal containing information about underlying neural and muscle activity. It has seen use in a wide variety of applications including gesture recognition [13], human-machine interfaces [14, 15], advanced prostheses [16], and medical diagnoses [17]. These applications require high channel count and spatially diverse recordings in order to capture the wide array of possible movements [18]. Moreover, these systems rely on continuous EMG recording and therefore require an unobtrusive recording platform which can be used chronically without user fatigue or discomfort.

The most common method of recording EMG is using electrodes placed on the surface of the skin which capture the activity of muscles below the recording electrode. While surface EMG (sEMG) is a noninvasive and convenient method for recording muscle activity, it suffers from a number of sensor- and system-level issues which make it a subpar recording modality for the applications above.

sEMG records the potential at the surface of the skin generated by the electrical activity of muscles below, and sensing this voltage reliably is heavily dependent on maintaining good electrical contact between the electrode and the human skin. Sweat, hair, movement, and the layers of skin tissue underneath the electrode all increase the impedance of the electrode-skin interface and introduce motion artifacts which can affect the quality and robustness of the recorded EMG signals. The standard Ag/AgCl electrodes used for sEMG help to reduce motion artifacts and decrease electrode impedance, but rely on a hydrogel between the metal and skin which dries out over time and limits recordings to a few hours. Dry electrodes are one alternative to hydrogel-based wet electrodes and can be used long-term without the need for maintenance [50, 51], but this comes at the price of increased electrode impedance, a dependence of impedance on electrode application pressure, and increased

motion artifacts. Finally, the large separation between muscles and electrodes means that sEMG records a spatial average of the muscle activity below the electrode, creates challenges in isolating small or deep muscles, and introduces crosstalk from nearby muscles which can make gesture classification more difficult [52].

No matter the type of electrode used for sEMG, a major challenge for high channel count systems is connecting all electrodes to the recording hardware. Running a cable from each individual electrode quickly becomes obtrusive as the number of channels grows, for example for a gesture recognition application requiring tens of channels.

Recently, there have been a number of systems that have attempted to address some of these issues. In [53], a robust system is demonstrated which relies on a custom screen-printed and flexible 64-channel electrode array to record sEMG and perform gesture classification. Despite promising results in terms of EMG signal fidelity, the system requires application of hydrogel on each electrode to reduce motion artifacts and causes skin irritation and sweating, both of which limit the long-term viability. Most importantly, neither of these solutions address the issues of recording from deep muscles and reducing crosstalk and therefore cannot be reliably used in applications where fine motor control is required.

Intramuscular EMG (iEMG) is another technique for recording EMG which consists of percutaneous needle or wire electrodes which record from inside the muscle. While this method provides high fidelity, highly selective EMG data, it is painful, prone to infection, and not suitable for long-term use. Methods to record iEMG using surface electrodes exist but have not been shown to be viable for long-term recordings [54].

The last approach that has been effective in providing chronic EMG recording is recording from inside the muscle or near the epimysium (the tissue surrounding muscles) using implanted electrodes. The IMES system [55] is one of the only implantable EMG systems demonstrated in humans to control an advanced prosthetic hand [56]. It consists of up to 32 individual single-channel recording implants placed inside muscles and powered by an external coil worn around the arm which provides inductive energy. It is worth noting that the particular setup used in their clinical trials only consisted of six implants, for reasons not stated in the work. Additionally, implants must reside within the volume covered by the external inductive power coil and therefore the spatial coverage of the system is limited. In addition, the relatively long length of each implant (16 mm) prevents recording from short muscles.

The Myoplant [6] is a more recent implantable system which consists of a relatively large (38mm by 25 mm by 8mm) central implant and a thin film electrode array used to reach muscles near the central implant. Each implant can only record from 5 electrodes (4 channels and a reference) and a dedicated external coil is required for every implant in order to provide wireless power, limiting the total number of channels and spatial coverage of the system. Various other systems have been developed and demonstrated *in vivo* without widespread adoption [57, 58, 59].

This chapter introduces the EMGnode system, a platform for recording EMG chronically and subcutaneously. This system aims to address the issues present with existing EMG recording modalities, namely to provide a platform for multi-channel, chronic EMG recording

with large spatial coverage, reduced motion artifacts, high selectivity, and the ability to record from deep muscles, without the need for obtrusive interconnects among recording sites. The system consists of a variable number of implants placed underneath the skin and fat, able to record and transmit a single channel of EMG data which is digitized and sent via passive backscatter to an external transceiver. The external transceiver is designed to optimally provide inductive power across a large area where the implants may reside [29]. The chapter begins with a discussion of EMG signal origins and requirements for an implanted system. Then, the overall system architecture and the multi-coil wireless power transfer (WPT) scheme are described. Next, the specific design of the implant and external transceiver are outlined in detail, motivating the design choices. Benchtop measurement results are provided to display basic functionality of each subsystem. Finally, conclusions are drawn and various avenues for improvement in future systems are proposed.

4.2 Recording EMG Subcutaneously

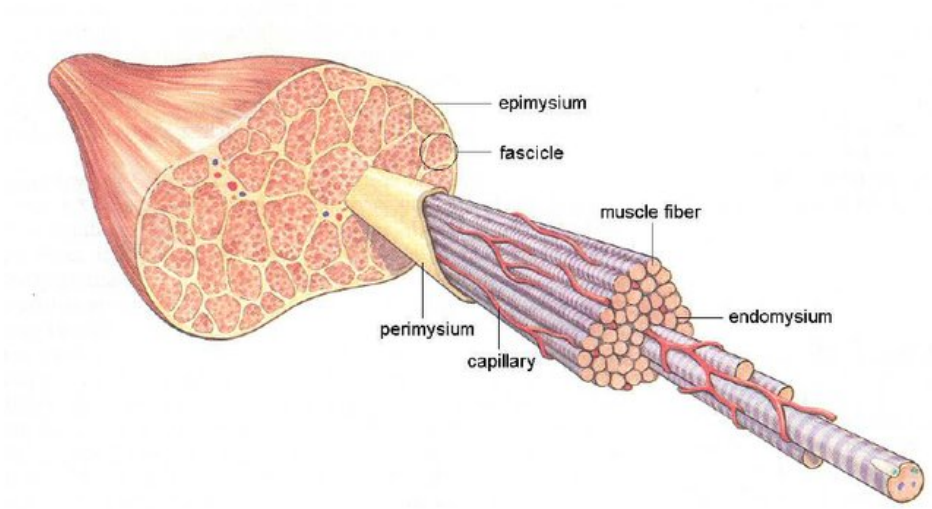

Figure 4.1: Skeletal muscle structure showing the epimysium surrounding bundles of muscle fibers. Image reproduced from [60].

Skeletal muscles consist of bundles of muscle fibers called fascicles held together by connective tissue. Figure 4.1 shows an illustration of a muscle and the various components which make up its structure. Muscle fibers (also called motor fibers, or MFs) are the contractile units within a muscle and are responsible for translating intention and neural signals into mechanical motion. Motor fibers are innervated by motor neurons, which originate in the brainstem or spinal cord and connect directly to muscles in order to activate them. This activation transforms a single neural action potential (AP) into hundreds or thousands of motor

unit action potentials (MUAPs), effectively amplifying the neural signal in order to move large muscles. The number of muscle fibers and motor neurons within a muscle determine its size, strength, and endurance. For example, a small muscle such as Lumbricalis I (used to flex the metacarpophalangeal joints in the hand) has around 10,000 muscle fibers and around 90 motor neurons, for an innervation ratio of 110. On the other hand, a larger and stronger muscle such as the Temporalis (a muscle on the side of the head used for chewing) can have over 1.5 million muscle fibers and 1,150 motor neurons, leading to an innervation ratio of 1,300 [61]. In addition to determining the strength of the muscles, the innervation ratio is an important determinant of the type, shape, and amplitude of EMG signals generated during muscle contraction.

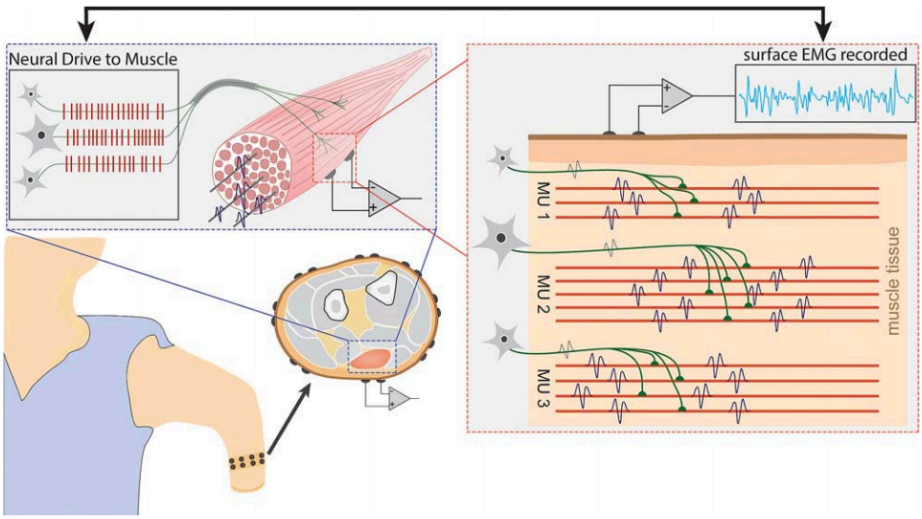

Figure 4.2: Generation and recording of EMG from the surface of the skin. Image reproduced from [62].

EMG recordings detect the electrical potentials generated by muscle cells as they are activated. An action potential from one or multiple motor neurons innervates hundreds or thousands of motor fibers. These motor fibers generate their own action potentials called motor unit action potentials (MUAPs) and traverse along the direction of the muscle fiber at a propagation speed of 2-10 m/s [63]. During surface EMG recording, electrodes placed on the surface of the skin sense the aggregate voltage generated from these propagating dipoles. The result is a summation of hundreds or thousands of MUAPs, either from the same muscle but distinct muscle fibers, or from completely separate muscles. Figure 4.2 shows an illustration of the EMG signal origin and recording.

4.2.1 Requirements for Recording Subcutaneous EMG - Implant Constraints

The goal of the EMGnode system presented in this chapter is to record chronic EMG from multiple distinct regions of the forearm. The system consists of multiple, randomly distributed, single-channel recording nodes implanted under the skin and fat, in direct contact with muscle. Each node receives energy through an inductive WPT link, records a channel of EMG data via a pair of on-board electrodes, and transmits this data to an external transceiver. The following assumptions are made and used to guide the initial design of the WPT link:

a) Implant volume should be minimized to reduce tissue damage from implantation.

b) The system is limited to using commercial off-the-shelf (COTS) components in order to demonstrate a cheap and general purpose prototype which can be further optimized in future generations.

c) The power dissipation of the implant is approximately 2 mW, based on available ICs and the minimum functionality required for each implant.

d) The implant is located underneath 2mm skin and 2mm fat, with 10mm of muscle underneath. There is an additional 1mm of air between the skin and any external TX coil.

The primary design decision and constraint for such an implantable system is the size of the implant, which affects the wireless power efficiency, recorded signal to noise ratio (SNR), and thermal characteristics of the system. The design begins by considering various effects on the size and shape of the implanted nodes, which drive the circuit design for the rest of the system.

4.2.1.1 SNR Limitations

Unlike traditional surface EMG which measures an electrical potential differences between a recording site and a "distant" reference, both the recording and common electrode of an EMGnode implant must be on the same footprint. As the size of the implant decreases, so does the inter-electrode distance (IED) and the amplitude of the recorded EMG signal. It is obvious that below a certain IED the recorded EMG signal will have an amplitude below the noise floor. Assuming equal vertical distance from each electrode to the MF, the two electrodes sense the same dipole voltage but with a shift in time dependent on the IED and propagation velocity, as shown in the left of Figure 4.3. As such, there exists an optimal time shift between the two waveforms where the maximum positive voltage recorded by electrode 1 aligns with the maximum negative voltage recorded by electrode 2. Figure 4.3 shows a few example time domain waveforms for a recording setup consisting of a pair of 1 mm^2 electrodes 1 mm away from a MF with a single MUAP. As the IED increases, the differential

amplitude increases as well (right), peaking at the optimal IED and then decreasing as the differential voltage approaches two non-overlapping dipole waveforms. The same analysis is performed for different vertical distances between electrodes and MFs and this is shown in Figure 4.4, which shows the amplitude of a differentially recorded MUAP as a function of IED for various vertical offsets between the muscle and recording electrodes.

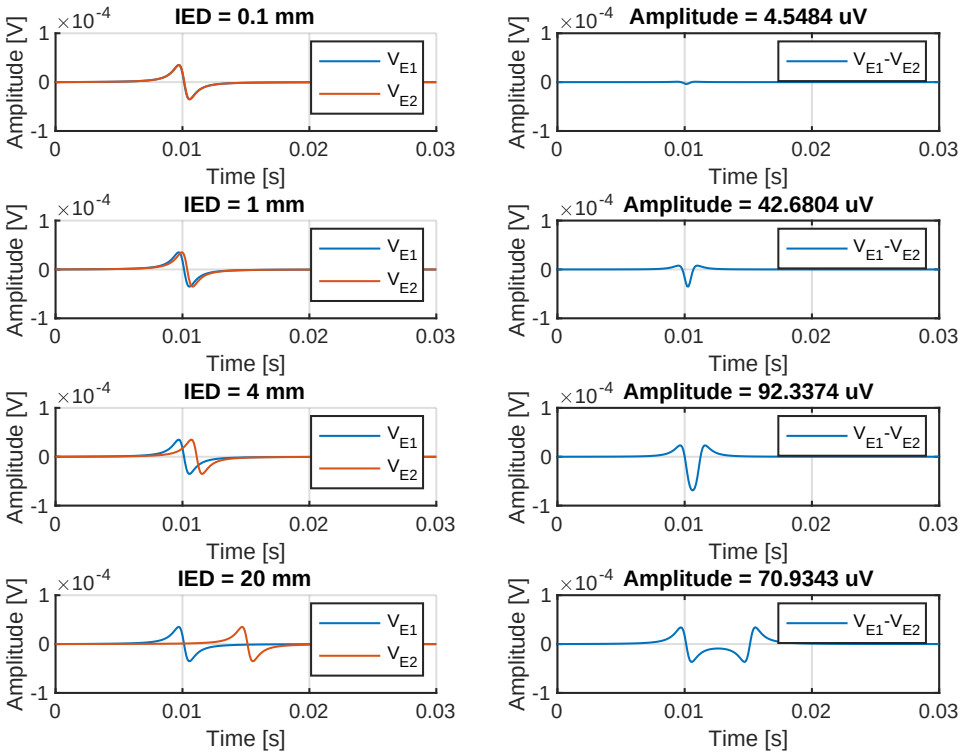

Figure 4.3: Simulated time domain voltage waveforms for a differentially recorded MUAP. Both electrodes are 1 mm away from the MF, the MUAP travels at 4 m/s, and the IED ranges from 0.1 mm to 20 mm.

In order to characterize the effect of IED on recorded EMG amplitude, a simulation model partly based on [64] was created in MATLAB (Mathworks) and used to simulate various EMG recording setups, as shown in Figure 4.5. The motor unit action potential (MUAP) is modeled as a current dipole traveling along a muscle fiber (MF) and originating from a location in the middle of the MF, shown by the axon connection in Figure 4.5. The model assumes a single motor unit (MU) innervating a single motor fiber (MF) that is located at the top of the muscle of interest closest to the recording electrodes, but the model is easily extendable to multiple MUs and any innervation ratio in order to adjust the amplitude of EMG signal. The media is chosen to be 2mm of skin, 2mm of fat, and 10mm of muscle. A pair of electrodes are modeled as a random distribution of point sources within a 1mm by 1mm area in order to account for finite electrode size. The position of these electrodes relative to

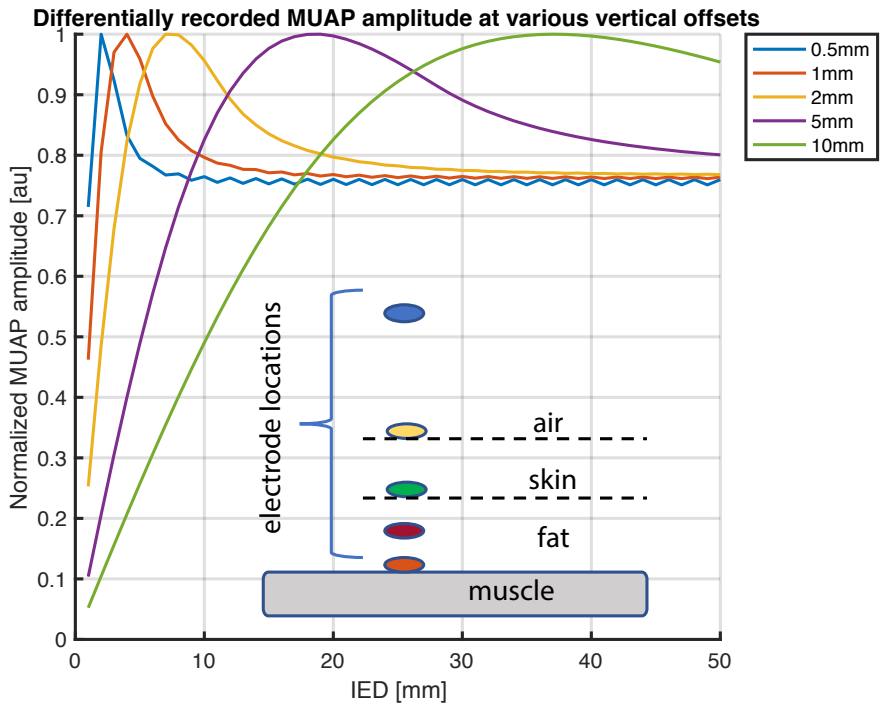

Figure 4.4: Simulated normalized MUAP amplitude as a function of IED for various vertical distances between muscle and electrodes (see inset). There exists an optimum IED for each vertical distance.

each other (IED) and relative to the muscle (y) is swept in order to find the optimum IED (IED_{opt}) for each vertical distance to the MF. Conduction velocity is assumed to be 4 m/s, the thickness of the epimysium (t_e) is 50 µm, and the thickness of an individual MF (t_{MF}) is 50 µm. Figure 4.6 shows the result of this simulation, which shows that IED_{opt} is linearly proportional to the distance between the electrodes and MF. For the case of implanted EMG recording along the forearm where the distance between electrodes and MF is on the order of a few mm, IED_{opt} is between 2mm and 6 mm. Note that, although large muscles may have MFs which are farther away from the epimysium, the EMG signal is dominated by the MFs closest to the electrodes since the measured dipole voltage is proportional to $1/r$. Thus, an implant optimized for maximum SNR while recording differential EMG near the muscle has an ideal size of at most 6 mm per side, depending on exact geometry and electrode locations. Lastly, these results confirm the popular choice of 20mm IED for sEMG [65, 66].

4.2.1.2 PCB Fabrication Technology Limitations

A second limiting factor on the size of the implant is particular to a COTS design, as the minimum area of the implanted PCB is ultimately determined by the size of available components and PCB technology. The EMGnode is designed to minimize the number of

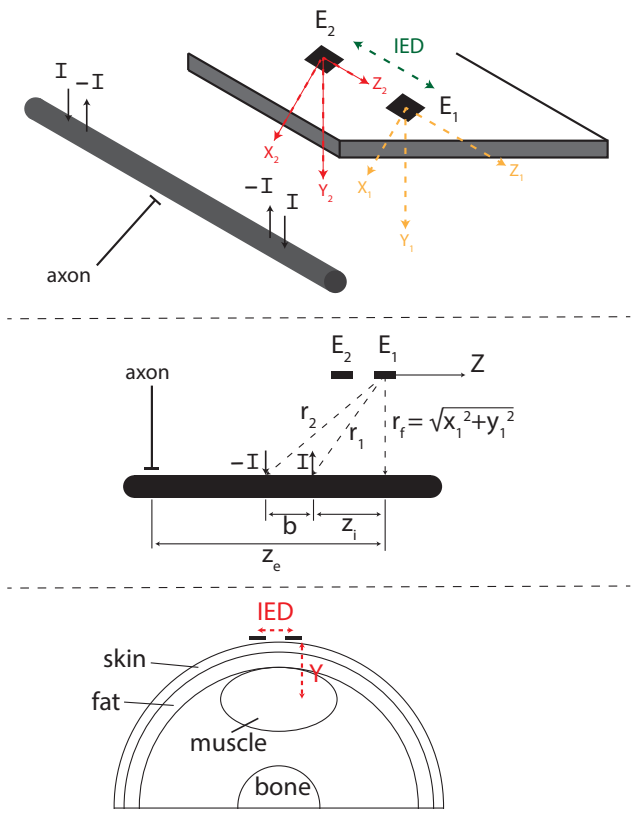

Figure 4.5: EMG modeling setup. Illustrations adapted from [64].

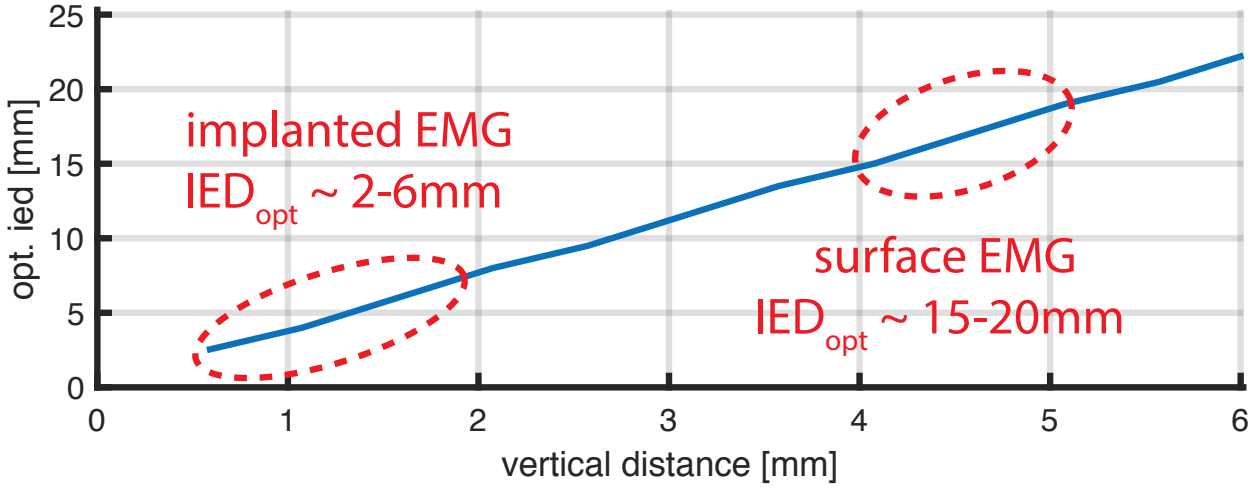

Figure 4.6: Optimum IED as a function of vertical distance between muscle and recording electrodes.

components in order to minimize component area and routing. Furthermore, IC components were specifically chosen based on the available packages from various manufacturers, with a particular emphasis on those available in chip-scale packages. The smallest possible design consists of 5 ICs and 29 passives for a total component area of 27.81 mm^2. Assuming a standard 4-layer PCB with components on both sides and taking into account standard routing and clearance constraints, the minimum area of an EMGnode is approximately 30 mm^2.

4.2.1.3 Thermal Limitations

Prior work in [67] has shown that a 5 mm by 6 mm implanted IC causes temperature to linearly increase with slopes of 0.051 °C/mW and 0.089 °C/mW with and without blood perfusion, respectively. Thus, to operate safely below the 1 °C maximum allowable tissue heating [68], a 5 mm by 6 mm implant can dissipate a maximum of 19.6 mW assuming there is blood flow around it. Without blood perfusion, this limit is lower (11.2 mW), but still an order of magnitude greater than the expected power dissipation of a single EMGnode. Since the size of the COTS implant is limited to about 30 mm^2, tissue heating effects do not impose a limitation on the size of the implants.

4.2.1.4 SAR Limitations

A secondary tissue heating effect is caused by electromagnetic (EM) radiation from the external coil which must comply with specific absorption rate (SAR) limits. SAR is a measure of the rate of RF energy absorption by the human body and has a maximum limit based on a maximum allowable tissue heating of 1 °C. The FCC defines upper limits for SAR based on whole-body measurements and partial-body averaging, as well as for specific frequencies. For biomedical implants operating above a few hundred kHz, these limits are 0.08 W/kg and 1.6 W/kg for whole-body and partial-body, respectively [68]. Since inductive WPT links operate in the near-field, it is sufficient to consider the partial-body average of 1.6 W/kg, measured across a 1 g of tissue, when designing links. The European SAR limits of 2 W/kg averaged over 10 g of tissue are less strict, but the US limits are used throughout this thesis.

SAR is proportional to the E-field and is related by

$$SAR = \frac{\sigma |E|^2}{\rho} \tag{4.1}$$

where σ is the conductivity of the tissue, E is the rms electric field strength, and ρ is the mass density of the tissue. For WPT links, SAR is determined by the E-field generated by the TX coil(s) which is directly proportional to the link efficiency and amount of power required to be transmitted by the TX to ensure RX operation. Since the efficiency of an inductive WPT link decreases with decreasing RX size, there exists a lower limit on the RX size below which the required TX power exceeds the SAR limit of 1.6 W/kg.

To investigate this limit for the particular application of implanted EMG in the forearm, Ansys HFSS simulations were performed for a variable-sized, single-turn RX placed underneath 1mm of air, 2mm of skin, and 2mm of fat, with 10mm of muscle underneath. The RX trace width was kept at a constant ratio of the total side length in order to maintain a constant fill ratio. The RX is powered by a single-turn hexagonal TX with 30 mil trace width, sized for maximum efficiency and operated at the optimum frequency for WPT (see Section 2.2). As the RX decreases in size, the TX power is increased in order to harvest 2 mW of power at the RX, and the peak average SAR averaged over 1 g of tissue is shown to increase. At an RX size of 0.1 mm, the maximum SAR value is exceeded, indicating that the smallest RX that can be powered with this particular geometry is between 0.1 mm and 0.25 mm in size. These results are shown in Figure 4.7.

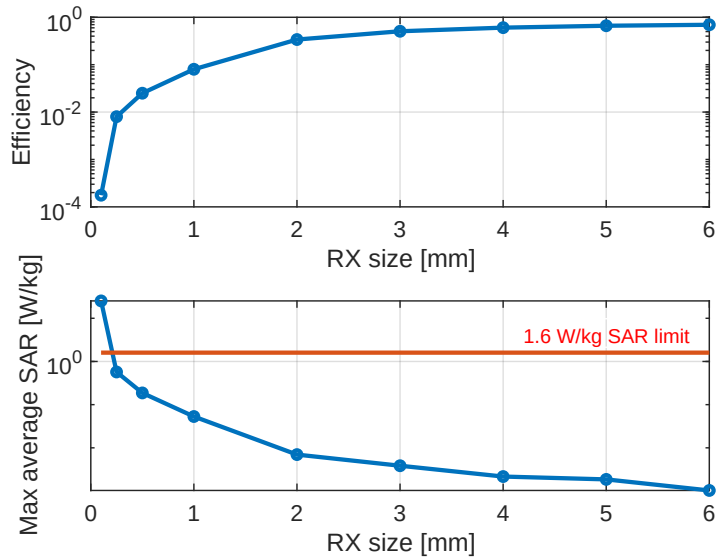

Figure 4.7: Maximum achievable WPT efficiency (top) and peak average SAR as a function of RX size.

Thus, the implant size is mainly constrained by the particular COTS implementation to approximately 6 mm by 6 mm, which is also the ideal IED for maximum SNR EMG recording. An implementation with this constraint serves as a reasonable proof-of-concept system, but the secondary effects discussed (heating, SNR, SAR) must be carefully considered when moving to an ASIC implementation.

4.3 EMGnode System Architecture

The EMGnode system, as envisioned in Figure 4.8, consists of a variable number of implanted single-channel EMG recording nodes and an external transceiver responsible for wireless power delivery and control. A single 6 mm by 6 mm EMGnode is shown in Figure 4.8(b) which consists of a four-layer standard printed circuit board (PCB) containing the recording electrodes, inductive power transfer coil, and associated circuitry. The EMGnodes are designed to be placed under the skin and fat of the forearm, directly in contact with the epimysium, as shown in Figure 4.8(c). This enables chronic use, reduces motion artifacts, and allows recording from deeper and smaller muscles not easily accessible with traditional surface EMG techniques. The design of the implant is discussed in more detail in Section 4.3.1.

The external transceiver (Figure 4.8(d)) is a PCB containing a three-layer tessellation of hexagonal loops designed to generate a homogeneous magnetic field at the location of the implants [29]. It is responsible for demodulating the backscatter data from multiple nodes and transmitting it via a Bluetooth Low Energy (BLE) link to an external logging device (e.g. laptop or phone) using the on-board radio system-on-chip (SoC). The design of the external transceiver is discussed in more detail in Section 4.3.2.

Figure 4.9 shows the block diagram of the entire EMGnode system with a single implant shown for clarity. Each implant contains a power receiving coil, L_{RX}, which is responsible for harvesting inductive energy from the external transmitter. A parallel capacitor C_{RX} sets the resonant frequency, while an RF-DC rectifier in combination with a voltage regulator generates a stable DC voltage for the microcontroller and amplifier. The recorded EMG signal is amplified, filtered, digitized, and used to drive a switch in parallel with the coil in order to perform passive backscatter. This modulated data is recovered at the primary coil, demodulated, and digitized by a microcontroller on the transceiver, and further relayed to an external logging device via Bluetooth. Multiple data streams from implants are backscattered at variable programmable frequencies and demodulated at the transceiver so that a single external coil array can address multiple implants.

The external transceiver provides wireless power by driving a coil array, L_{TX}, with a class-E power amplifier (PA) designed for maximum efficiency. The transceiver also manages the power delivery to multiple implants through a simple closed-loop algorithm. Each implanted node monitors its received and rectified DC voltage through a voltage divider and appends a few bits onto the header of a data transmission in order to alert the transceiver if it is receiving too much, too little, or just enough power. The transceiver is able to modulate the transmitted power using a switching DC-DC regulator to vary the supply voltage of the on-board class-E PA. This scheme ensures that the implants generate a steady supply with maximum efficiency, as will be discussed in Section 4.3.1.

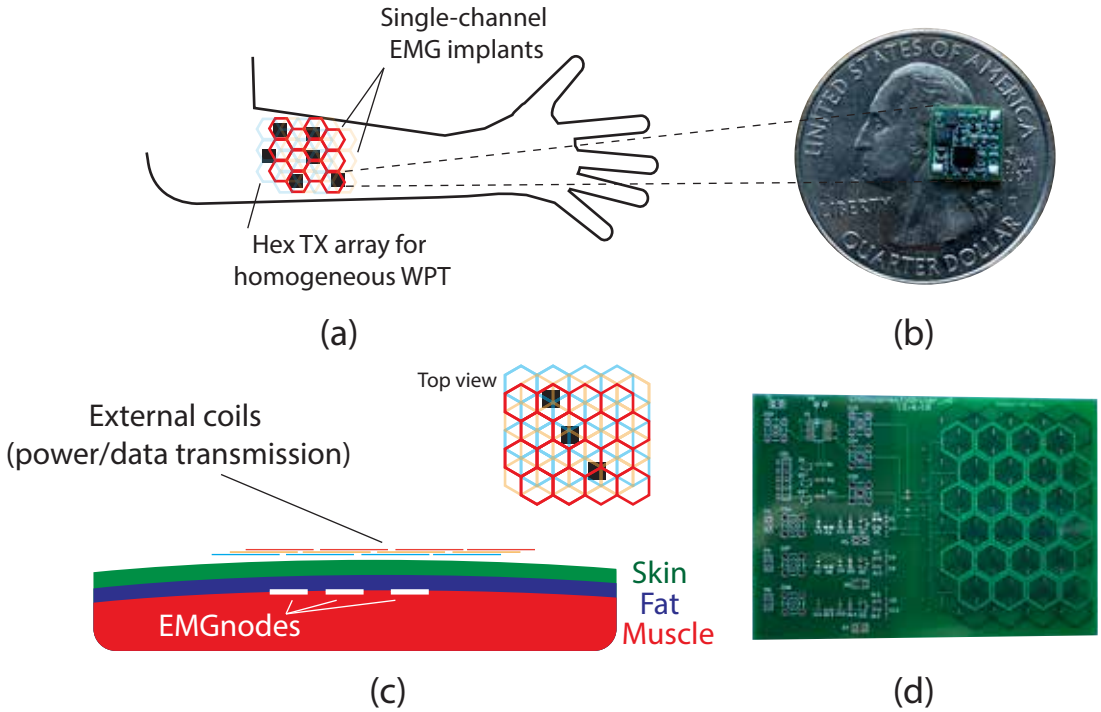

Figure 4.8: (a) The concept of a distributed EMGnode system for recording EMG data from multiple locations along the forearm; (b) EMGnode implant board with US quarter for scale; (c) cross section of system showing multiple implanted EMGnodes that receive energy through a transcutaneous inductive link; (d) external transceiver coil array.

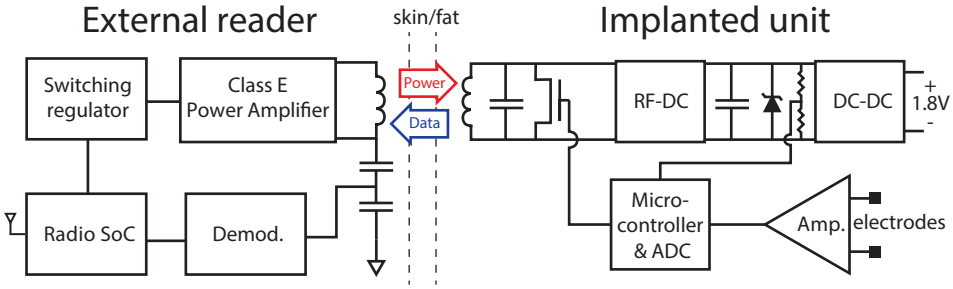

Figure 4.9: Block diagram of the EMGnode system.

4.3.1 Implant Design

Each EMGnode implant is able to record a single channel of EMG, digitize the data, and relay it to the external transceiver through a passive backscatter link. All implants are identical and operate from a single 1.8 V supply generated on-board, consuming 1.23 mW. The

following section describes the implant in greater detail and provides benchtop measurement results.

4.3.1.1 EMG-recording Front-End

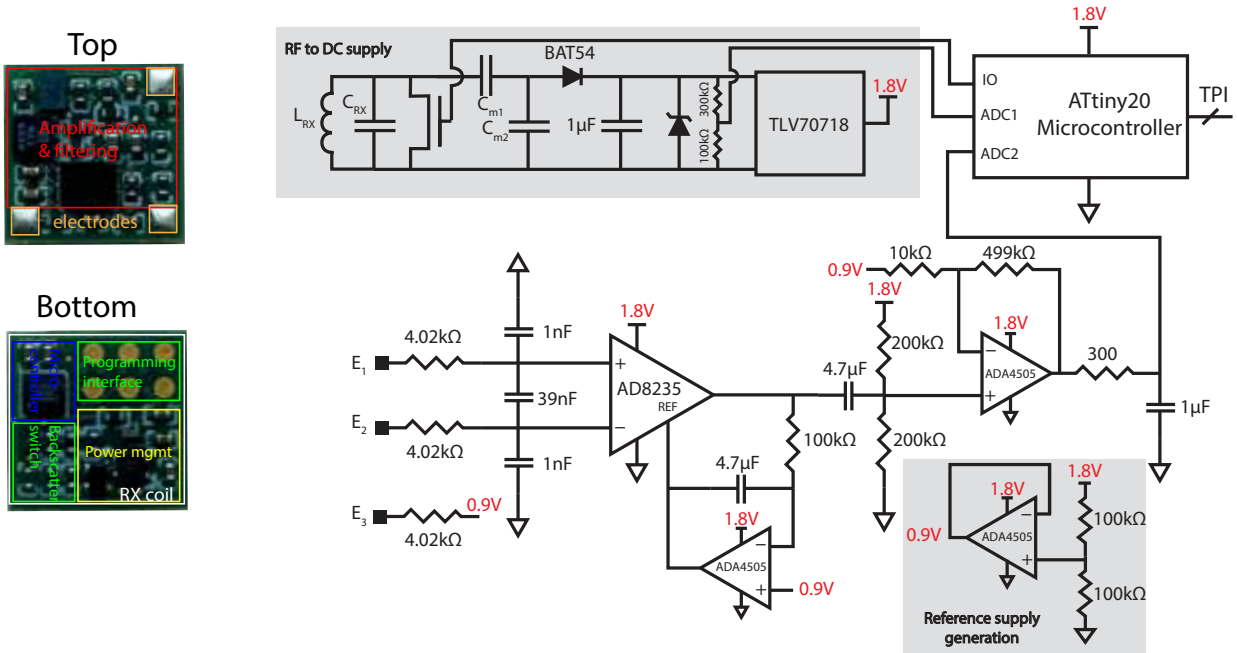

Figure 4.10: PCB photo of the front and back of a 6 mm by 6 mm EMGnode implant (left) and schematic of the EMGnode implant (right).

The schematic diagram of a single implant is shown in Figure 4.10. A pair of 1 mm by 1 mm copper electrodes are used to record a single channel of EMG at the muscle interface underneath the layers of fat and skin, while a third electrode optionally biases the body at mid-supply. The µV level signals picked up from these electrodes are first amplified by an instrumentation amplifier (in-amp) (Analog Devices AD8235) with gain of 5. This instrumentation amplifier was chosen for its low power (72 µW) and small form-factor (1.5 mm by 2.2 mm wafer level chip scale package [WLCSP]).

The input filter structure before the instrumentation amplifier rejects radio frequency (RF) rectification which can couple into the in-amp and present as a DC offset at the output, potentially railing the amplifier. While the AD8235 has a high common mode rejection ratio (CMRR) at low frequencies (100 dB at 1Hz and 60dB at 60Hz), its CMRR at frequencies above a few kHz is relatively low. The input filter sets the common mode and differential

mode bandwidth to

$$f_{DM} = \frac{1}{2 \cdot \pi \cdot 4.02k\Omega \cdot (2 \cdot 39nF + 1nF)} = 501Hz \tag{4.2}$$

$$f_{CM} = \frac{1}{2 \cdot \pi \cdot 4.02k\Omega \cdot 1nF} = 39.6kHz. \tag{4.3}$$

The differential filter capacitor (39 nF) is chosen to be larger than the common mode filter capacitor (1 nF) in order to minimize common mode to differential mode conversion due to common mode capacitor mismatch.

AC-coupling of the input is achieved through a feedback loop: an op-amp integrator (Analog Devices ADA4505) drives the reference terminal of the in-amp, creating a high-pass filter without the need for input coupling capacitors which can degrade the common-mode rejection of the amplifier due to component variations.

An op-amp (Analog Devices ADA4505) provides a second stage of gain. Filtering is performed throughout the signal chain and includes: (1) a 501 Hz low-pass filter at the input of the instrumentation amplifier, (2) a 0.34 Hz high-pass filter formed by an integrator driving the reference input of the instrumentation amplifier, (3) a 0.32 Hz high-pass filter formed by the 4.7 µF capacitor and 200 kΩ resistors, (4) and a 530 Hz anti-aliasing low-pass filter before the ADC. Figure 4.11 shows the simulated and measured frequency response of the front-end. The total gain is adjustable via the feedback resistor of the second op-amp and corresponds to 29.5/34.8/48.1 dB with a 3-dB bandwidth between 0.5 Hz and 489/525/422 Hz, respectively. The amplifier is limited by the op-amp gain bandwidth product of 50kHz, so a tradeoff exists between bandwidth and gain. However, even with the highest gain setting of 48.1 dB, the upper 3-dB frequency is high enough to capture high quality EMG signals, whose power spectral density is concentrated between tens of Hz to approximately 500 Hz.

Figure 4.12 shows the simulated and measured voltage noise spectral density as a function of frequency. The in-band input-referred noise is 3.10 µVpp and is dominated by the instrumentation amplifier.

To demonstrate full functionality of the recording front-end, EMG signals were captured using an EMGnode testboard and standard gel electrodes. The testboard contained the same basic circuitry as the EMGnode implant but on a larger PCB with various testpoints and peripheral components. All relevant ICs were either identical to the final form-factor version, or were the same part but in an alternate package to ease assembly and testing. In particular, the AD8235 instrumentation amplifier was replaced with an AD8236 which is identical but housed in an 8-lead MSOP which allowed for manual assembly. Similarly, the ADA4505 operational amplifier on the testboard were a quad configuration in a single 14-lead TSSOP package and the ATtiny20 microcontroller came in a 14-lead SOIC. The testboard and test setup is shown in Figure 4.13(b).

EMG was recorded from the flexor digitorum superficialis (FDS) muscle which runs along the anterior of the forearm and is responsible for flexing the finger joints and wrist joint. A pair of Ag/AgCl EMG electrodes (Covidien Kendall) were used. These electrodes have a diameter of 24 mm and were spaced 48 mm apart (center to center). EMG signals were sensed,

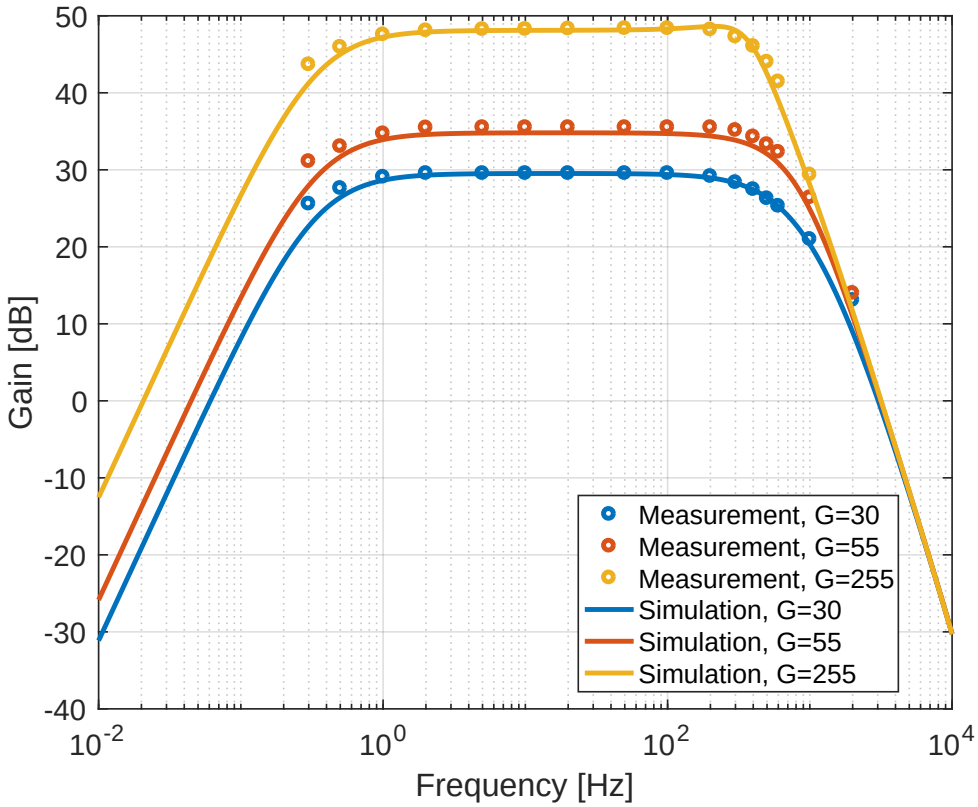

Figure 4.11: Simulated and measured frequency response of the EMGnode implant front-end for three different gain settings.

amplified, filtered, digitized, and Miller modulated by the on-board microcontroller. To simplify testing, the testboard was DC powered using a lab supply and the digitized backscatter data directly drove an I/O pin of an external microcontroller used for demodulation, as shown in Figure 4.13(a). Finally, Figure 4.13(c) shows the recorded EMG signal which is demodulated by the external microcontroller (Nordic nRF51) and displayed in real-time on a laptop. During the approximately 30 second test, the FDS muscle was flexed by squeezing the fist four times during the first 10 seconds, followed by six short flexions (taps) of the fingers wherein the four fingers closed into the palm in a grabbing motion. These gestures are all clearly visible in the recording with amplitudes ranging from 2 mV to 4.5 mV (input referred). Note that these EMG recordings were performed with surface electrodes and an IED of approximately 50 mm and the recorded signal amplitude and frequency content are not expected to match that of recordings using the final EMGnode implants. Instead, this experiment serves as a demonstration of the EMGnode recording sub-system and the ability to employ miniaturized EMGnode implants as part of a larger system, e.g. for a gesture recognition platform.

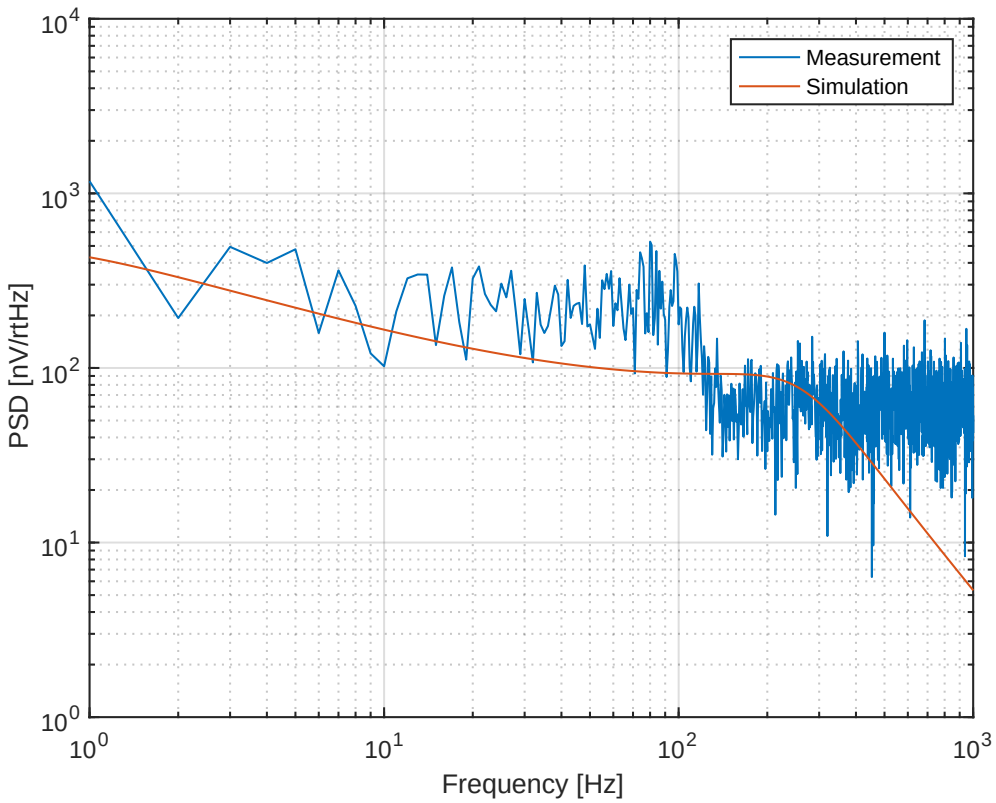

Figure 4.12: Voltage noise spectral density as a function of frequency of the EMGnode implant front-end, without the ADC.

4.3.1.2 AC Power Recovery

Inductive power is transmitted from the external coil array, picked up by the on-board 6 mm by 6 mm square coil, rectified (Diodes Inc. BAT54), and regulated to 1.8 V using a low-dropout (LDO) voltage regulator (Texas Instruments TLV707). Since the efficiency of the LDO is determined by the ratio of output to input voltages, it is imperative to maintain a voltage at the output of the rectifier around 1.8 V, so a voltage divider connected to the output of the rectifier and digitized by a separate ADC channel on the microcontroller is used to monitor the received voltage. This signal is sampled every 100 ms, encoded into two bits, and sent in the header of the backscattered data in order to adjust the TX power transmitted. A value of 00 corresponds to an acceptable received RF voltage (1.8-2.2V), 01 to a received voltage (2.2-2.8V), and 10 means it is much too high (>2.8V). Based on this signal, the TX adjusts the voltage of the class-E PA in order to increase or decrease the received voltage at the implant, as is discussed in the following section.

In order to minimize implant size, the inductive coil for WPT is wrapped around the elec-

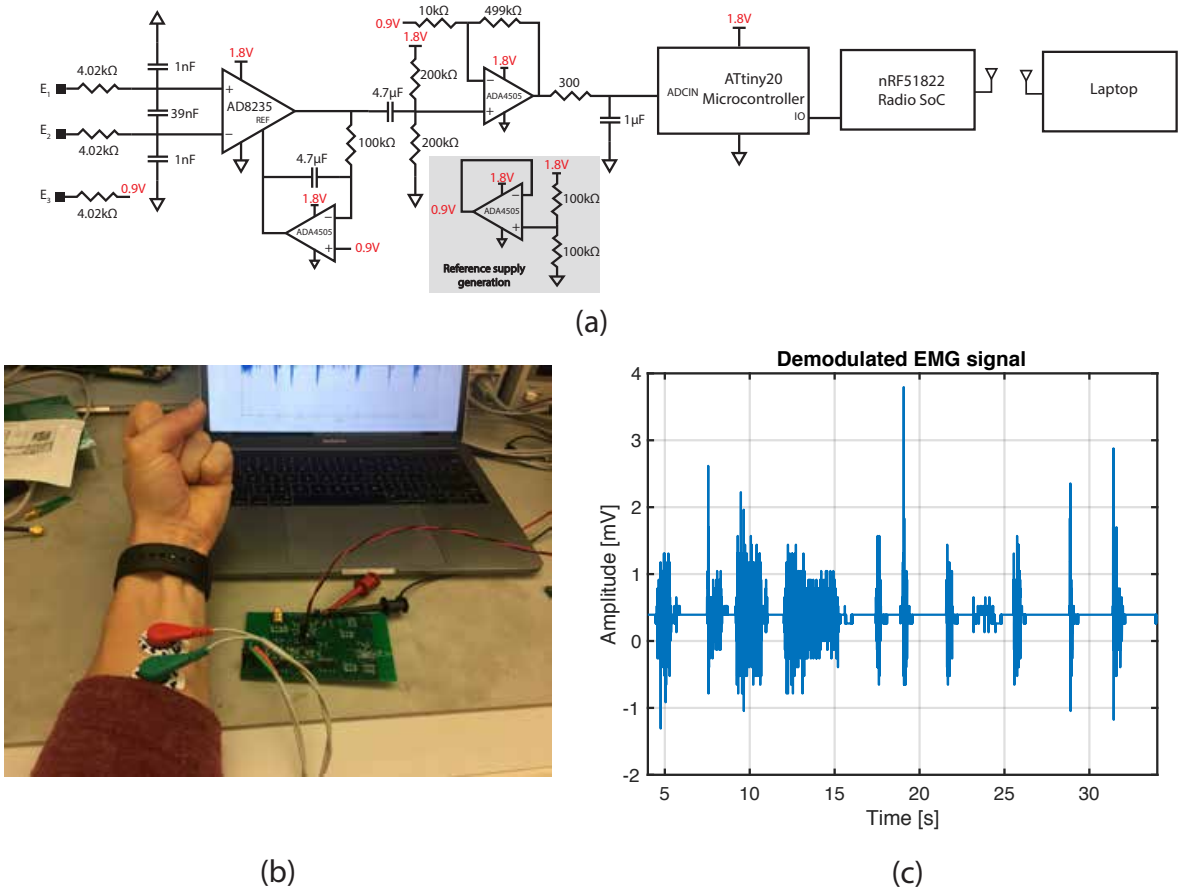

Figure 4.13: Test setup for measuring surface EMG using EMGnode testboard.

tronics. Due to this, the WPT efficiency is lowered due to two main factors - (1) components and routing inside the loop and (2) coil detuning and reduction in k due to ground/power planes. The first is addressed by using minimum width traces (3 mil), minimizing the number of components, and using the smallest footprint components available. The second issue is addressed by utilizing a star ground configuration instead of traditional power planes. The lack of ground and power planes underneath the entire board reduces RF rejection, supply decoupling capacitance, and complicates routing, but ensures a high efficiency by minimizing Eddy currents and maximizing the coupling coefficient k.

As a result, the WPT efficiency is reduced due to the components and routing inside of the inductive loop. Figure 4.14 shows the WPT efficiency for 3 different implant configurations. The ideal case is an inductive loop with no other metal traces or components nearby and achieves nearly 70% efficiency. On the other extreme, a coil with a metal ground plane underneath achieves a maximum efficiency of only 34.5% due to a significant decrease in Q and k and Eddy currents [69]. Lastly, the design used for the EMGnode implants achieves a moderate maximum efficiency of 56%.

In order to validate the HFSS simulation results for WPT efficiency, various testboards

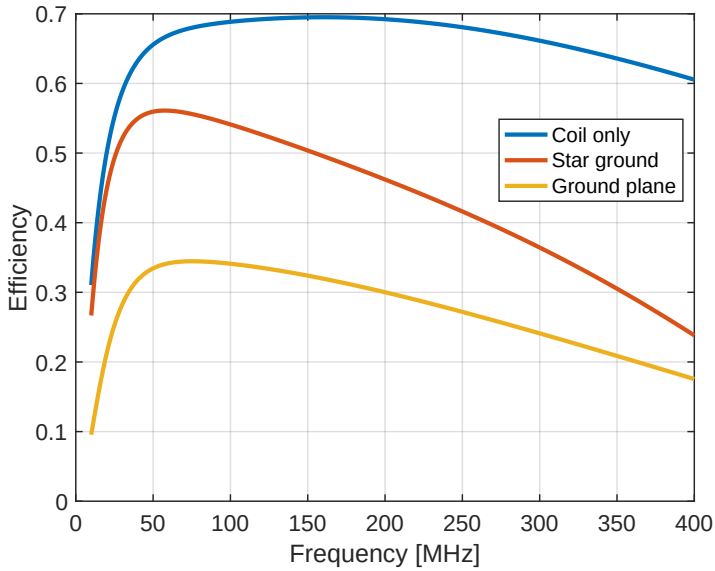

Figure 4.14: Effect of internal metallization on WPT efficiency. The ideal case of a simple loop with no traces or components nearby (blue) achieves a maximum efficiency of 69.5%. The case of a ground plane below the coil without any components (yellow) achieves a maximum efficiency of 34.5%. The implemented EMGnode implant has multiple components and traces within the loop and utilizes a star ground and achieves a maximum efficiency of 56% (red).

were fabricated specifically for measuring the WPT efficiency of different configurations. However, there is a tradeoff between ease of measurement and accuracy. For example, connecting the coils to instruments like a VNA requires traces from the coil to an SMA connector, which can decrease coil Q and impact the measured efficiency. Therefore, the HFSS models were updated to include all physical features of the testboards, with a goal of validating the agreement between simulations and measurements on the specific geometric setup. Gerber files of the designed PCBs were exported from Altium Designer and imported into HFSS as 3D geometries. HFSS's import functionality was found to be inaccurate, with incorrect rendering of geometries in the z-axis and no way to control for trace thickness, so a manual approach was taken in which each layer of the PCB was imported individually as a 2D sheet and thickened in the z-dimension using HFSS's geometry editor functionality. After all layers of the PCB were imported and thickened, any necessary corrections were made to vias and traces and a box of FR-4 was added to model the PCB material.

Simulations were performed in air to match the expected measurement setup. Performing measurements in tissue phantom (e.g. chicken meat or pig skin) is challenging, so was reserved for the final measurement setup only. As such, the results should not be interpreted

as the final efficiency of the EMGnode system, but as a sanity check that the measurements and simulations match. Figure 4.15(a) shows the measurement and simulation setup using the testboards. The RX testboard consists of a 6 mm by 6 mm square coil on a 2-layer PCB, with 9 mm traces connecting to the rest of the circuit for resonance, matching, optional rectification, and SMA connector. The TX testboard includes options for a single 12 mm hexagonal coil, a single layer tessellation, and a three layer tessellation. Each of these are routed to control circuitry and SMA connectors for testing.

To guarantee 5 mm separation between TX and RX coils, the TX board was held in place on a lab bench using plastic spacers while the RX board was clamped using a Helping Hands soldering station tool and held above the TX coil(s), with the distance verified using a ruler placed next to the RX board. SMA cables connected each coil to an Agilent N5242A Vector Network Analyzer (VNA). S-parameters were recorded across a frequency range of 10 MHz to 1 GHz and exported to MATLAB for post processing, where they were converted to circuit parameters and used to calculate the maximum efficiency as given by eq. (2.16). S-parameters were also exported for the same configuration in HFSS. Figure 4.15 shows the simulated and measured maximum achievable two-port efficiency as a function of frequency, which shows good agreement. The HFSS simulation (red) shows a slightly higher efficiency as the measured TX board resonated at a lower frequency due to additional parasitic capacitance from the SMA cable and connector. Note that these results are for the maximum achievable two-port efficiency and do not include any losses due to driver inefficiency or matching.

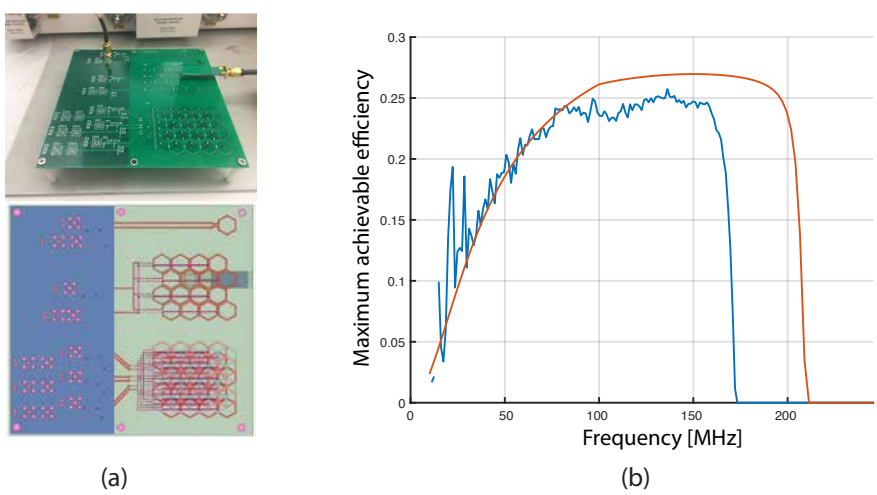

Figure 4.15: (a) Measurement and simulation setup for validating HFSS simulation accuracy in air. (b) Maximum achievable efficiency for two-coil link in air for simulation (red) and measurement (blue) showing good agreement.

4.3.1.3 Passive Backscatter Telemetry

The EMGnode system is designed to record EMG from multiple implants simultaneously in order to be used for applications such as gesture recognition. As such, it must support uplink communication from each implant to an external transceiver. Furthermore, any communication from an EMGnode implant must be simple and low-power in order to reduce the complexity, size, and power dissipation of the implanted node.

Passive backscatter telemetry is a method of communicating between an energy-constrained receiver and a transmitter, and is widely used in RFID tags to transmit small amounts of data from an RFID tag to an external reader. Energy is transmitted from the TX to the RX in a continuous wave (CW) and the RX modulates its data on top of this signal by intentionally mismatching its antenna (coil) impedance in order to reflect back a portion of the incident CW signal. By varying the antenna impedance - or equivalently shifting the RX resonance - the RX can encode digital signals onto the CW signal. This reflected energy is detected and demodulated at the TX in order to recover the data. Passive backscatter allows for communication to/from a battery-less device by piggy-backing on the existing wireless power link and requires only a single switch on the RX, thereby reducing complexity and minimizing RX power.

The EMGnode implant performs amplitude-shift keying (ASK) based passive backscatter by shifting the resonance frequency of its RX coil via switch M1 and capacitor $C_{backscatter}$ in Figure 4.16. Whenever the switch is turned on, the total resonance capacitance increases to $C_{RX} + C_{backscatter}$ and the resonance frequency decreases accordingly. Figure 4.17 shows SPICE simulation results of an example waveform across L_{RX} during normal operation and during a data transmission. The TX (not shown) is driven by a 160 MHz sine wave voltage and the coupling between TX and RX is 0.03. The 1 µF rectifier capacitor is large enough to maintain the output DC voltage when the switch is closed, so the regulated voltage is not affected during data transmissions. The ratio size of $C_{backscatter}$ relative to C_{RX} determines the ASK modulation ratio and the received backscatter waveform at the TX. In this simulation, C_{RX} is 48 pF and $C_{backscatter}$ is 5 pF and the modulation ratio is 0.66. $C_{backscatter}$ can be replaced by a 0 Ω resistor to change from ASK to on-off-keying (OOK), but this increases the ripple on the rectified voltage and can increase the power supply noise of the implant.

In order to address multiple nodes through a single external transceiver, the backscattered data from different nodes must be separated in time or frequency. While both time division multiplexing (TDM) and frequency division multiplexing (FDM) were considered, the EMGnode system utilizes FDM due to its higher accuracy and capacity. Miller and Manchester modulation are two modulation techniques frequency used in RFID applications to encode RFID tag baseband data and drive a backscatter switch. The two schemes are closely related, with Miller encoding consisting of a Manchester encoder followed by a flip-flop. Both schemes encode binary data as a transition from low-to-high or high-to-low (or in the case of Miller a lack of transition). In Manchester encoding, a 1 is represented as a low-high transition in the middle of the bit period and a 0 is represented as a high-low

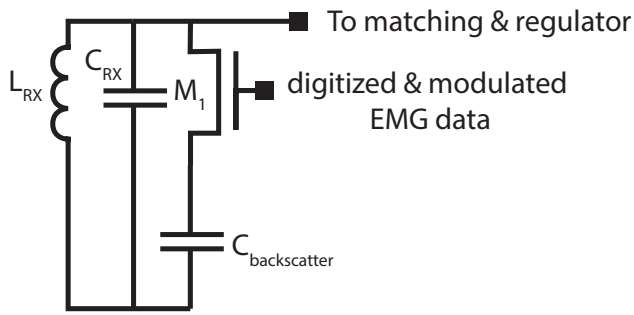

Figure 4.16: Passive backscatter is performed on each EMGnode implant through the use of switch M1 and capacitor $C_{backscatter}$. When the implant is not transmitting data, the switch is open and the link operates at resonance in order to maximize WPT efficiency. To transmit data, the on-board microcontroller drives the switch M1 with Miller modulated data at a pre-determined baseband frequency.

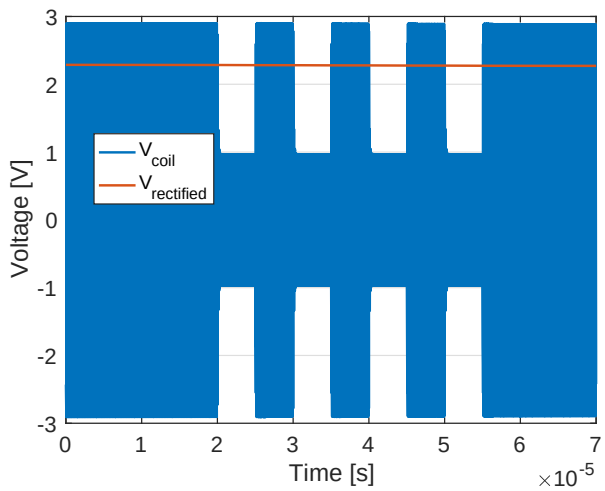

Figure 4.17: Voltage waveform at EMGnode RX. In blue is the received voltage which is rectified to generate the on-board DC supply, shown in red.

transition in the middle of the bit period (for the case of IEEE 802.3 convention; the opposite is true for the G. E. Thomas convention). In Miller encoding, the following rules apply:

a) If the bit is 0, the signal is not inverted.

b) If the bit is 0 but previous bit was also 0, the signal is inverted at the edge of the bit.

c) If the bit is 1, the signal is inverted at the middle of the bit.

In both cases, following the conventions allows to translate binary data into baseband Manchester/Miller data. This baseband encoded data can be multiplied by a square wave with

subcarrier frequency f_M in order to generate higher-order subcarrier modulation rates. An example of this is shown in Figure 4.18 for the case of Miller encoding. Note that for higher order Miller subcarriers, the Miller baseband transitions are encoded as phase inversions.

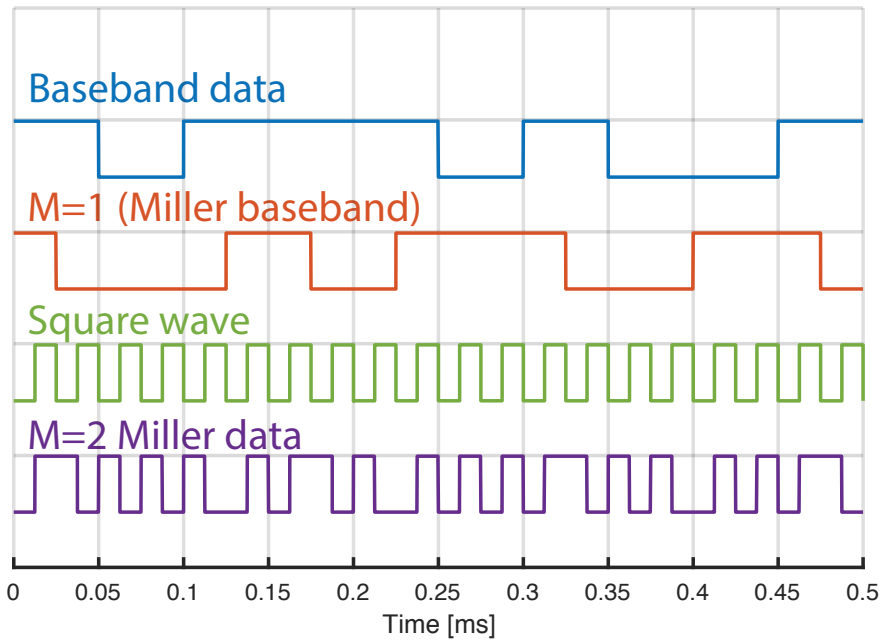

Figure 4.18: Example of Miller encoding from binary data (0x2E9) to Miller baseband and M=2 Miller.

Miller and Manchester encoding are relatively simple to implement in firmware, but Miller encoding was chosen for the EMGnode system as it has fewer transitions (about half that of Manchester) which reduces switching power on the implant, and because it utilizes less bandwidth. To illustrate the differences in spectral bandwidths between Manchester and Miller encoded data, a simple MATLAB encoder was designed to encode a 10-bit data sample into both Manchester and Miller data. Three individual EMGnodes are modeled performing Manchester/Miller modulation at subcarrier frequencies of 20 kHz, 40 kHz, and 60 kHz. Figure 4.19 shows the frequency spectra of these nodes for each modulation technique. The Manchester modulated data shows significant overlap among the three spectra which leads to bit errors when demodulating data unless the subcarrier frequencies are spaced far enough apart. On the other hand, the Miller data spectra do not overlap significantly, so Miller modulation is utilized in order to simplify demodulation.

The amplified and filtered EMG signal is digitized by a 10-bit analog-to-digital converter (ADC) on-board the microcontroller (Atmel ATtiny20) at a sampling rate of 1 KHz. This digitized baseband signal is Miller encoded at a programmable frequency (20 kHz, 40 kHz, ...) and used to drive a MOSFET switch (Texas Instruments CSD13380F3) which performs impedance modulation of the RF coil. In this way, multiple nodes can be powered

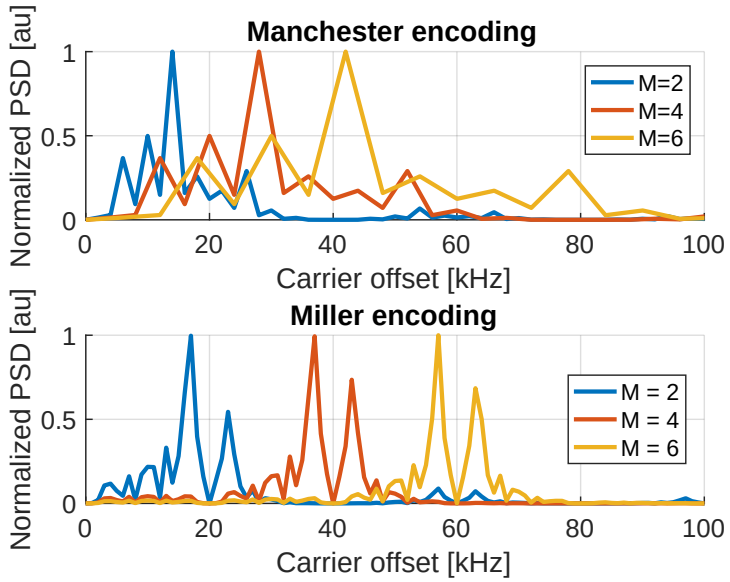

Figure 4.19: Frequency spectra of Manchester and Miller encoded backscatter data.

by and communicate with a single external TX array by selecting a unique backscatter frequency [24]. Each node modulates the baseband data with a unique backscatter frequency, chosen for optimum separation in the frequency domain. Demodulation occurs at the TX board through a custom demodulation algorithm which is discussed in the following section.

Figure 4.20 illustrates the concept of frequency division multiplexing (FDM) via programmable frequency Miller modulated backscatter for the case of four implanted EMGnodes. The baseband data (10 bits, 0x2E9) represents a sample of EMG data without packet headers for clarity. For simplicity, it is assumed that each EMGnode transmits the same packet. The baseband data is converted to Miller encoded data on the on-board microcontroller of each implant and used to drive the backscatter switch (Figure 4.20(a)). The combined backscatter from multiple nodes is received at the TX and its frequency spectrum is shown in Figure 4.20(b). At the TX, the received backscatter waveform is bandpass filtered to extract a specific EMGnode, digitized, and demodulated to reconstruct the baseband data (Figure 4.20(c)).

4.3.1.4 Implant Firmware

The implant microcontroller (ATtiny20) was selected for its extremely small footprint. It is available in a 12-ball 1.555 mm x 1.403 mm WLCSP package, does not require an external crystal oscillator, and is the smallest commercially available microcontroller that was available at the time of this work. Programming is performed using a 3-wire Tiny Programming Interface (TPI) which includes a RESET, TPICLK, and TPIDATA pin.

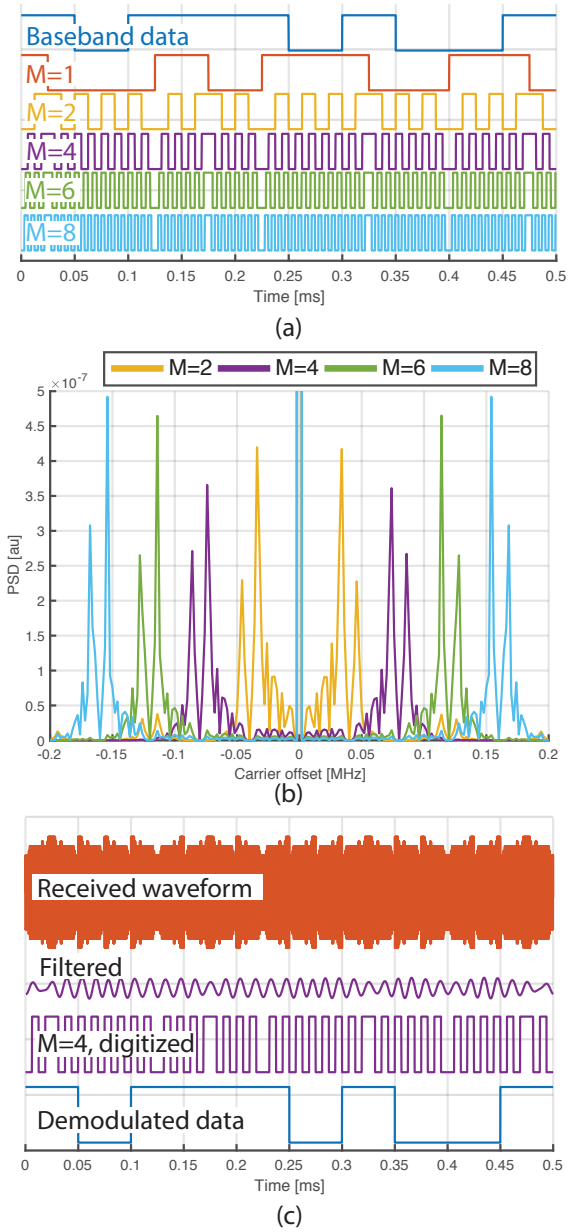

Figure 4.20: Illustration of multi-frequency Miller modulation for simultaneous passive backscatter communication from multiple implants. (a) Modulation of baseband data 0x2E9 into four Miller encoded waveforms with different carrier rates. (b) Frequency spectrum of the received backscatter waveform at the TX. (c) The received backscatter waveform is filtered and digitized in order to recover the original baseband data.

The ATtiny20 is an 8-bit AVR microcontroller supporting 112 RISC instructions, fully static operation, and up to 12 MIPS throughput at 12 MHz. It includes 2K bytes of in-system

programmable flash memory and 128 bytes of internal SRAM. 8-bit and 16-bit timer/counter peripherals support accurate timing for EMG sampling, while a 10-bit ADC is used to digitize the EMG data. A maximum speed of 4 MHz is achieved at a supply voltage of 1.8 V.

The ATtiny20 is responsible for digitizing EMG data, monitoring the received and rectified voltage, Miller encoding data, and driving the on-board MOSFET to perform passive backscatter. Fitting all of this functionality in a microcontroller with only 2 kilobytes of memory was a major challenge. A timer is used to trigger an ADC conversion every 1 ms, corresponding to a 1kHz sampling frequency. The result of this conversion along with any relevant header bits are packetized and converted into Miller data by selectively toggling an I/O port which drives the backscatter switch. Extensive loop unrolling is used to reduce code size to below the 2 kilobyte memory limit and the final code size is 1846 bytes. Finally, Figure 4.21 shows measurement results of Miller encoding on the ATtiny20 microctontroller. Continuous baseband data (in this case a reference voltage instead of EMG signal) is sampled using the ADC and encoded into Miller data.

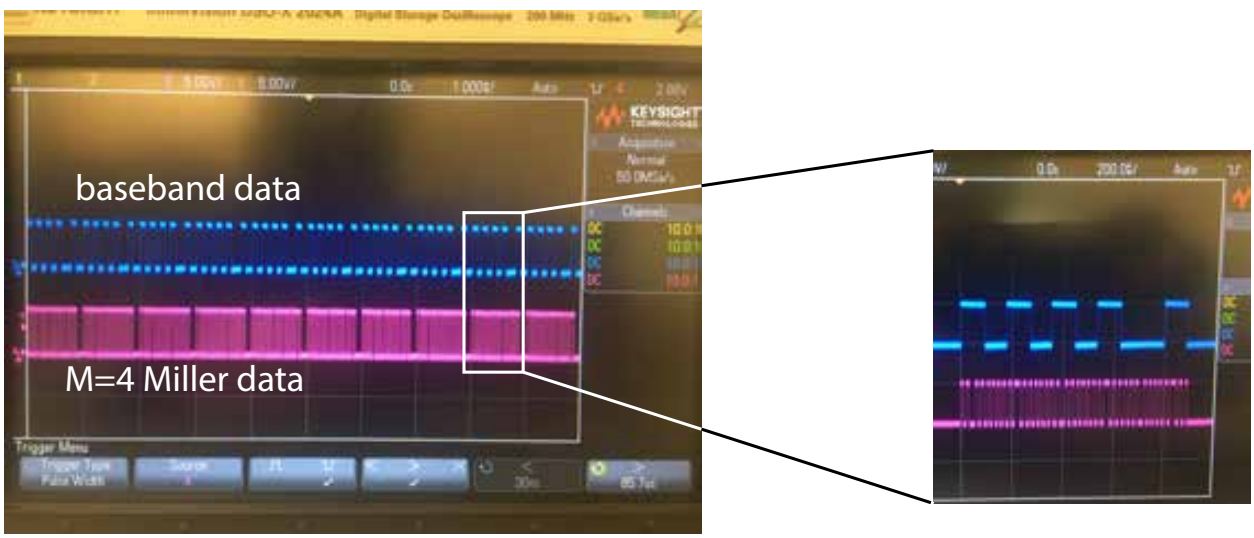

Figure 4.21: Oscilloscope measurement of Miller encoding using ATtiny20 microcontroller.

Programming of the ATtiny20 occurs via a Tag-Connect programming cable (TC2030-IDC-NL) and a custom 6 landing pad footprint on the PCB (refer to Figure 4.10). In order to decrease area, the through hole guide holes of the Tag-Connect programmer were omitted. The programming cable was destructively modified by removing the guide pins and manually held during programming. While this worked well for a few boards, future iterations of the implants should consider an alternate programming header. One alternative that was explored but not realized is the use of breakaway tabs to hold programming and test headers. This would allow for various test points and peripheral test circuitry to be included as part of the implant and detached after programming. A line of through holes (sometimes called mouse bites) provide a natural breakpoint for the tabs and allow the required test and

programming signals to be routed from the main board to the header on the breakaway tab. In order to minimize the potential for trace lift-off, shorts, and board delamination during breakaway, vias are placed near the breakaway point to create a natural blocking of the shear stresses. Additionally, the traces themselves are thinner at the breakaway point, so that the stresses are concentrated in that location and the traces break cleanly. However, due to the small size of the PCB and the potential for board damage, this option was not utilized in this prototype version.

4.3.2 External Transceiver Design

Various prototypes of the transceiver were fabricated throughout this work. These prototypes, along with function generators and a VNA, were used to demonstrate functionality of the power and data link. While the focus of this work is not on the design of the external transceiver (except for the coil array), the following sections briefly summarize the relevant pieces of the proposed final TX board. The schematic of the TX is shown in Figure 4.22.

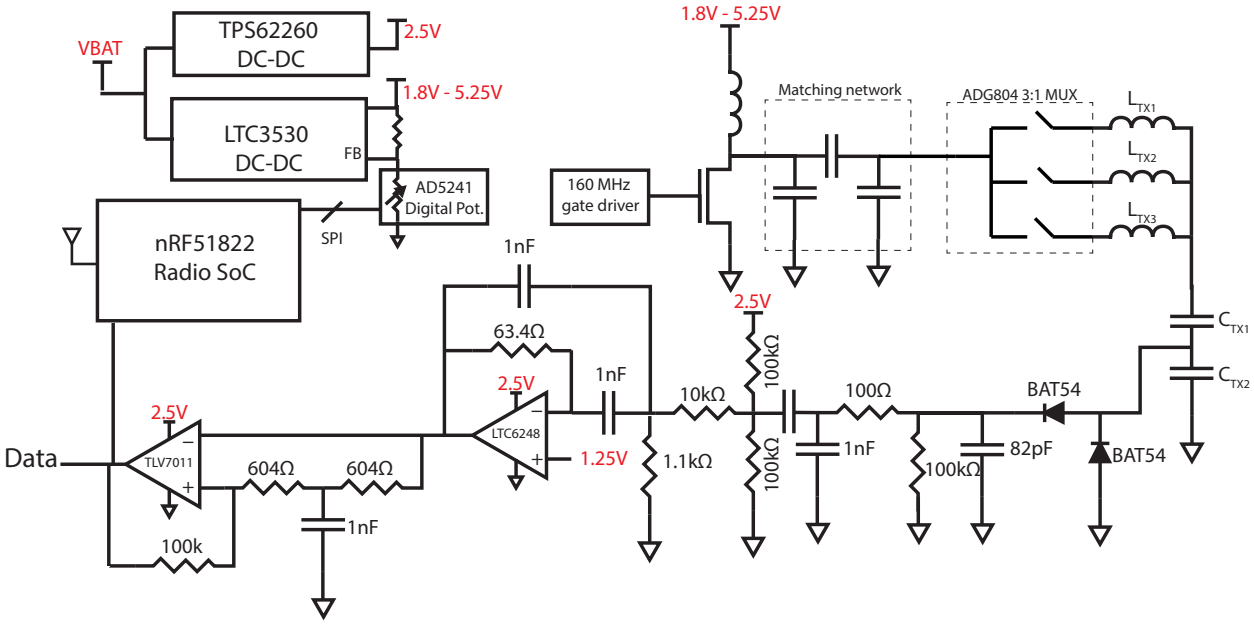

Figure 4.22: Schematic of the proposed external TX.

The TX provides power to the implants via a 160 MHz inductive link. An oscillator and gate driver drive the gate of a MOSFET switch in a class-E power amplifier configuration. The class-E PA is supplied by a variable supply generated by a DC-DC converter (Analog Devices LTC3530) whose output voltage is tuned by a digital potentiometer (Analog Devices AD5241) and has a range of 1.8 V to 5.25 V. This allows for real-time digital adjustment of PA output power in order to ensure the correct power is transmitted to the implants. A

single PA is optionally switched among the three layers of coils in TDM fashion using a 3:1 multiplexer (Analog Devices ADG804) in order to generate a homogeneous magnetic field, as discussed in Chapter 3.

Demodulation is performed by tapping off the RF signal through a capacitive divider and performing envelope detection, filtering, amplification, and digitization. The RF carrier is filtered out and the resulting data is bandpass filtered and digitized using a comparator (Texas Instruments TLV7011). This digital bitstream is fed into a microcontroller (Nordic nRF51822) where further filtering and digital demodulation is performed.

Finally, the TX contains a radio SoC (Nordic nRF51822) which performs the demodulation and sends the data to a logging device such as a PC. The radio also controls the digital potentiometer through SPI in order to adjust the supply and transmit power of the class-E PA. Additionally, it controls the mux to select the appropriate TX coil layer.

4.4 System Measurements

Unfortunately, due to external circumstances final system measurements were not able to be completed. The EMGnode implant and TX PCBs were designed, fabricated, and assembled but were not received before the entire university was shut down in accordance with health and safety regulations related to Covid-19. As a result, this chapter includes measurements taken during the design and initial testing of the system, but these do not include any measurements with the final form factor (6 mm by 6 mm) EMGnode implants.

The following performance characterizations are planned:

a) WPT efficiency using final form-factor EMGnode implant and TX array.

b) WPT homogeneity above single- and three-layer arrays. This measurement can only be accurately done using the final form-factor EMGnode implant, as the testboard is too large and would perturb the magnetic field around the array.

c) Multi-node backscatter. Testing was done on the prototype implant to demonstrate the ability to perform Miller modulation at different frequencies. Additionally, MATLAB- and microcontroller-based demodulation was performed for multiple backscatter nodes. However, because the backscatter relies on the WPT link being operational for multiple implants, it was impossible to perform this measurement until the very end.

d) System-level EMG recording using 6 mm by 6 mm EMGnode implants. Measurements were only performed using prototype boards and surface electrodes.

These measurements will be performed as soon as it is safe to do so, and a paper submitted for publication detailing the full system.

4.5 Summary

A system of distributed EMG-recording implants called EMGnodes was presented. This system addresses the issues present with existing surface EMG recording modalities by providing a platform for multi-channel, chronic EMG recording with large spatial coverage and reduced motion artifacts. The system consists of a variable number of implants underneath the skin and fat of the forearm which record a single channel of EMG data, digitize, encode, and transmit it through a passive backscatter communication link.

The implant was optimized in terms of size to maximize the recorded EMG signal while achieving higher WPT efficiency and operating under various safety constraints. Each implant contains an analog front-end for recording a single channel of EMG data, a microcontroller for digitization and control, and an RX coil for inductive WPT operation. The implant was realized using COTS components and each implant is 6 mm by 6 mm in size.

The EMGnode platform serves as a proof of concept of the inductive WPT methodology developed in the previous chapters. Custom TX coil arrays were fabricated and used to power multiple EMGnode implants and HFSS simulation and measurement results were provided throughout. Some measurements are still pending and a second generation of the implant and external transceiver are planned.

Chapter 5

Conclusions

5.1 Contributions

The contributions of this thesis are two-fold. First, an analysis of inductive wireless power transfer to implanted devices is presented, including a design methodology for maximum efficiency powering of small, shallow implants inside the body. A novel approach to powering distributed implants is presented, which utilizes two dimensional tessellations of sub-coils to generate a homogeneous magnetic field in the location of the implants. This allows for wirelessly powering of multiple implants without requiring knowledge of their locations, complex beamforming, or real-time tracking.

Secondly, this thesis introduces the EMGnode system, a platform for multi-channel, chronic EMG recording with large spatial coverage. The EMGnode platform is, to the author's knowledge, the smallest implantable EMG system. This system demonstrates the multi-implant WPT technique in a realistic application and is able to power multiple EMGnode implants with a single external coil and without requiring knowledge of the locations of the implants.

5.2 Extensions and Future Work

No work is ever truly complete and the unfortunate timing of the end of the this degree and thesis coinciding with a national shut-down due to Covid-19 makes that particularly true. In large part due to a lack of access to lab space and equipment, a lot of planned work was not able to be performed. In particular, a lot of final system measurements were not done. So, while the EMGnode system exists, its functionality has not been verified in the final form-factor version.

There are a number of key measurements that will be taken in the coming months, after the completion of this thesis, and submitted for publication. These include full system measurements for the EMGnode platform, including multi-receiver WPT and backscatter data transmission and demodulation from multiple nodes using a single TX. Additionally, it

would be very interesting to integrate the EMGnode system into the HD gesture recognition platform developed in [53] by replacing the flexible screen printed array with a number of EMGnodes for a more chronic system.

In terms of extensions to the EMGnode system, further scaling of the system in terms of size and power is the main goal. Going to a custom implementation of the implant would allow for a decrease in area of 10x and a decrease in power of 100x, based on rough estimates. This would create a system that is truly implantable and chronic. It would also introduce other limitations in terms of SAR and SNR as the size of the implant decreases, potentially creating different bottlenecks to what is presented in this work.

Another key piece missing from this work is in-vivo studies of the EMGnode implants. The EMG signal at the expected location of the implants was modeled but not verified, so an important next step is to take EMG recordings from a rat or non human primate (NHP) in order to demonstrate in-vivo functionality. Accomplishing this would require either an acute system for recording subcutaneous EMG, or the packaging and implantation of an EMGnode implant.

Finally, the design of the external transceiver system should be fleshed out. For this thesis, the TX coils were driven directly with signal generators or network analyzers, as the focus was on demonstrating the ability to power randomly distributed implants. However, it would be useful to build a fully functional external transceiver board which includes coils, RF drivers, computation, and telemetry capabilities in order to demonstrate a fully functional EMGnode system.

5.3 Critical Assessment

Finally, a reflection on this work as a whole. There were two main goals that the author hoped to accomplish with this research: to introduce a novel method of powering distributed implants and to develop a prototype system for chronic EMG that demonstrates this powering technique. The results presented in Chapter 3 are promising in terms of the first goal, where a technique for designing inductive WPT links for distributed implants was presented and verified.

The second goal of developing a prototype of the EMGnode system was lofty but well constrained. There is certainly a lot of improvements that can be made to the system proposed in Chapter 4, but it is a good initial step. Due to the limited time and resource constraints of the project - which for the most part was a solo effort - the focus was on getting a working prototype. This enabled a realistic use-case application and allowed for the multi-RX WPT link to be validated in a real system. However, a lot of further optimization of the system is possible. An ASIC implementation of the implant would reduce size and power. A re-design of the EMG electrodes may allow for higher fidelity EMG recordings. A fully realized external transceiver would allow for a more complete system demonstration. The TX coil arrays should be implemented in a flexible process so that they better conform to

the shape of the forearm. This would require more extensive modeling of the effects of bend on the coil characteristics and WPT link efficiency and homogeneity.

Bibliography

[1] UN DESA. "World Population Prospects 2019: Highlights". In: *New York (US): United Nations Department for Economic and Social Affairs* (2019).

[2] Omid G Sani et al. "Mood variations decoded from multi-site intracranial human brain activity". In: *Nature biotechnology* 36.10 (2018), pp. 954–961.

[3] Jan M Rabaey. "The Human Intranet–Where Swarms and Humans Meet". In: *IEEE Pervasive Computing* 14.1 (2015), pp. 78–83.

[4] *Medtronic*. URL: `https://www.medtronic.com/`.

[5] *Neuropace*. URL: `https://www.neuropace.com/`.

[6] Soeren Lewis et al. "Fully implantable multi-channel measurement system for acquisition of muscle activity". In: *IEEE Transactions on Instrumentation and Measurement* 62.7 (2013), pp. 1972–1981.

[7] David C Bock et al. "Batteries used to power implantable biomedical devices". In: *Electrochimica acta* 84 (2012), pp. 155–164.

[8] Achraf Ben Amar, Ammar B Kouki, and Hung Cao. "Power approaches for implantable medical devices". In: *sensors* 15.11 (2015), pp. 28889–28914.

[9] Janko Katic, Saul Rodriguez, and Ana Rusu. "A high-efficiency energy harvesting interface for implanted biofuel cell and thermal harvesters". In: *IEEE Transactions on Power Electronics* 33.5 (2017), pp. 4125–4134.

[10] Dejan Rozgić and Dejan Marković. "A miniaturized 0.78-mW/cm2 autonomous thermoelectric energy-harvesting platform for biomedical sensors". In: *IEEE transactions on biomedical circuits and systems* 11.4 (2017), pp. 773–783.

[11] Jayant Charthad et al. "A mm-sized implantable medical device (IMD) with ultrasonic power transfer and a hybrid bi-directional data link". In: *IEEE Journal of solid-state circuits* 50.8 (2015), pp. 1741–1753.

[12] Dongjin Seo et al. "Wireless recording in the peripheral nervous system with ultrasonic neural dust". In: *Neuron* 91.3 (2016), pp. 529–539.

[13] Xu Zhang et al. "A framework for hand gesture recognition based on accelerometer and EMG sensors". In: *IEEE Transactions on Systems, Man, and Cybernetics-Part A: Systems and Humans* 41.6 (2011), pp. 1064–1076.

[14] Jeong-Su Han et al. "Human-machine interface for wheelchair control with EMG and its evaluation". In: *Proceedings of the 25th Annual International Conference of the IEEE Engineering in Medicine and Biology Society (IEEE Cat. No. 03CH37439)*. Vol. 2. IEEE. 2003, pp. 1602–1605.

[15] Yue H Yin, Yuan J Fan, and Li D Xu. "EMG and EPP-integrated human–machine interface between the paralyzed and rehabilitation exoskeleton". In: *IEEE Transactions on Information Technology in Biomedicine* 16.4 (2012), pp. 542–549.

[16] Claudio Castellini and Patrick van der Smagt. "Surface EMG in advanced hand prosthetics". In: *Biological cybernetics* 100.1 (2009), pp. 35–47.

[17] Erik Stålberg and Peter Dioszeghy. "Scanning EMG in normal muscle and in neuromuscular disorders". In: *Electroencephalography and Clinical Neurophysiology/Evoked Potentials Section* 81.6 (1991), pp. 403–416.

[18] Christoph Amma et al. "Advancing muscle-computer interfaces with high-density electromyography". In: *Proceedings of the 33rd Annual ACM Conference on Human Factors in Computing Systems*. ACM. 2015, pp. 929–938.

[19] Todd A Kuiken et al. "Targeted muscle reinnervation for real-time myoelectric control of multifunction artificial arms". In: *Jama* 301.6 (2009), pp. 619–628.

[20] Hunter Hanzhuo Wu et al. "A review on inductive charging for electric vehicles". In: *2011 IEEE international electric machines & drives conference (IEMDC)*. IEEE. 2011, pp. 143–147.

[21] SY Hui. "Planar wireless charging technology for portable electronic products and Qi". In: *Proceedings of the IEEE* 101.6 (2013), pp. 1290–1301.

[22] Kush Agarwal et al. "Wireless power transfer strategies for implantable bioelectronics". In: *IEEE Reviews in Biomedical Engineering* 10 (2017), pp. 136–161.

[23] John C Schuder. "Powering an Artificial Heart: Birth of the Inductively Coupled-Radio Frequency System in 1960". In: *Artificial organs* 26.11 (2002), pp. 909–915.

[24] William Biederman et al. "A Fully-Integrated, Miniaturized (0.125 mm^2) 10.5 μW Wireless Neural Sensor". In: *IEEE Journal of Solid-State Circuits* 48.4 (2013), pp. 960–970.

[25] Rikky Muller et al. "A minimally invasive 64-channel wireless μECoG implant". In: *IEEE Journal of Solid-State Circuits* 50.1 (2014), pp. 344–359.

[26] Wasif Khan et al. "Inductively coupled, mm-sized, single channel optical neuro-stimulator with intensity enhancer". In: *Microsystems & nanoengineering* 5.1 (2019), pp. 1–12.

[27] *Wireless Power Transfer*. URL: `https://en.wikipedia.org/wiki/Wireless_power_transfer#Inductive_coupling`.

[28] Ada SY Poon, Stephen O'Driscoll, and Teresa H Meng. "Optimal frequency for wireless power transmission into dispersive tissue". In: *IEEE Transactions on Antennas and Propagation* 58.5 (2010), pp. 1739–1750.

[29] George Alexandrov and Jan M Rabaey. "Wireless Power Transfer to Randomly Distributed Implants via Homogeneous Magnetic Fields". In: *2019 IEEE Biomedical Circuits and Systems Conference (BioCAS)*. IEEE. 2019, pp. 1–4.

[30] Huyen Le, Neric Fong, and Howard Cam Luong. "RF energy harvesting circuit with on-chip antenna for biomedical applications". In: *International Conference on Communications and Electronics 2010*. IEEE. 2010, pp. 115–117.

[31] Dukju Ahn and Maysam Ghovanloo. "Optimal design of wireless power transmission links for millimeter-sized biomedical implants". In: *IEEE transactions on biomedical circuits and systems* 10.1 (2015), pp. 125–137.

[32] Quang-Thang Duong and Minoru Okada. "Maximum efficiency formulation for multiple-input multiple-output inductive power transfer systems". In: *IEEE Transactions on Microwave Theory and Techniques* 66.7 (2018), pp. 3463–3477.

[33] Jonas Thelin et al. "Implant size and fixation mode strongly influence tissue reactions in the CNS". In: *PloS one* 6.1 (2011).

[34] *Nevro Omnia*. URL: `https://www.nevro.com/English/us/providers/omnia/default.aspx`.

[35] *Advanced Bionics*. URL: `https://advancedbionics.com/ca/en/home/products/hires-ultra-cochlear-implant.html`.

[36] Uei-Ming Jow and Maysam Ghovanloo. "Design and optimization of printed spiral coils for efficient transcutaneous inductive power transmission". In: *IEEE Transactions on biomedical circuits and systems* 1.3 (2007), pp. 193–202.

[37] Sarah E Cameron et al. "In vivo ultrasonic measures of skin layer thicknesses at various body locations and postures". In: *Medical Imaging 2018: Ultrasonic Imaging and Tomography*. Vol. 10580. International Society for Optics and Photonics. 2018, 105801B.

[38] Paul Störchle et al. "Measurement of mean subcutaneous fat thickness: eight standardised ultrasound sites compared to 216 randomly selected sites". In: *Scientific reports* 8.1 (2018), p. 16268.

[39] Inhee Lee et al. "An ultra-low-power biomedical chip for injectable pressure monitor". In: *2015 IEEE Biomedical Circuits and Systems Conference (BioCAS)*. IEEE. 2015, pp. 1–4.

[40] Sérgio Francisco Pichorim and Paulo José Abatti. "Design of coils for millimeter-and submillimeter-sized biotelemetry". In: *IEEE Transactions on Biomedical Engineering* 51.8 (2004), pp. 1487–1489.

[41] Toni Bjorninen et al. "Design of wireless links to implanted brain–machine interface microelectronic systems". In: *IEEE Antennas and Wireless Propagation Letters* 11 (2012), pp. 1663–1666.

[42] Maysam Ghovanloo and Suresh Atluri. "A wide-band power-efficient inductive wireless link for implantable microelectronic devices using multiple carriers". In: *IEEE Transactions on Circuits and Systems I: Regular Papers* 54.10 (2007), pp. 2211–2221.

[43] PA Hasgall et al. "IT'IS Database for thermal and electromagnetic parameters of biological tissues". In: *Version 3.0* (2015).

[44] Benjamin L Cannon et al. "Magnetic resonant coupling as a potential means for wireless power transfer to multiple small receivers". In: *IEEE transactions on power electronics* 24.7 (2009), pp. 1819–1825.

[45] Kisong Lee and Dong-Ho Cho. "Analysis of wireless power transfer for adjustable power distribution among multiple receivers". In: *IEEE Antennas and Wireless Propagation Letters* 14 (2015), pp. 950–953.

[46] S Abdollah Mirbozorgi, Pyungwoo Yeon, and Maysam Ghovanloo. "Robust wireless power transmission to mm-sized free-floating distributed implants". In: *IEEE transactions on biomedical circuits and systems* 11.3 (2017), pp. 692–702.

[47] Byunghun Lee, Dukju Ahn, and Maysam Ghovanloo. "Three-phase time-multiplexed planar power transmission to distributed implants". In: *IEEE journal of emerging and selected topics in power electronics* 4.1 (2015), pp. 263–272.

[48] Jihun Lee et al. "Wireless power and data link for ensembles of sub-mm scale implantable sensors near 1GHz". In: *2018 IEEE Biomedical Circuits and Systems Conference (BioCAS)*. IEEE. 2018, pp. 1–4.

[49] SY Ron Hui and Wing WC Ho. "A new generation of universal contactless battery charging platform for portable consumer electronic equipment". In: *IEEE Transactions on Power Electronics* 20.3 (2005), pp. 620–627.

[50] Amanda C Myers, He Huang, and Yong Zhu. "Wearable silver nanowire dry electrodes for electrophysiological sensing". In: *Rsc Advances* 5.15 (2015), pp. 11627–11632.

[51] Pascal Laferriere, Edward D Lemaire, and Adrian DC Chan. "Surface electromyographic signals using dry electrodes". In: *IEEE Transactions on Instrumentation and Measurement* 60.10 (2011), pp. 3259–3268.

[52] Dario Farina, Roberto Merletti, and Roger M Enoka. "The extraction of neural strategies from the surface EMG". In: *Journal of applied physiology* 96.4 (2004), pp. 1486–1495.

[53] Ali Moin et al. "An EMG gesture recognition system with flexible high-density sensors and brain-inspired high-dimensional classifier". In: *2018 IEEE International Symposium on Circuits and Systems (ISCAS)*. IEEE. 2018, pp. 1–5.

[54] Nikolay S Stoykov et al. "Recording Intramuscular EMG signals using surface electrodes". In: *9th International Conference on Rehabilitation Robotics, 2005. ICORR 2005*. IEEE. 2005, pp. 291–294.

[55] Richard F Weir et al. "Implantable myoelectric sensors (IMESs) for intramuscular electromyogram recording". In: *IEEE Transactions on Biomedical Engineering* 56.1 (2009), pp. 159–171.

[56] Paul F Pasquina et al. "First-in-man demonstration of a fully implanted myoelectric sensors system to control an advanced electromechanical prosthetic hand". In: *Journal of neuroscience methods* 244 (2015), pp. 85–93.

[57] Eleftherios Kampianakis et al. "A dual-band wireless power transfer and backscatter communication approach for real-time neural/EMG data acquisition". In: *IEEE Journal of Radio Frequency Identification* 1.1 (2017), pp. 100–107.

[58] Marshal Dian Sheng Wong et al. "A chronic implantable EMG recording system with wireless power and data transfer". In: *2017 IEEE Biomedical Circuits and Systems Conference (BioCAS)*. IEEE. 2017, pp. 1–4.

[59] Daniel McDonnall et al. "Implantable multichannel wireless electromyography for prosthesis control". In: *2012 Annual International Conference of the IEEE Engineering in Medicine and Biology Society*. IEEE. 2012, pp. 1350–1353.

[60] Henry Gray. *Gray's Anatomy: Descriptive and Surgical. TP Pick, R. Howden, eds.* 1995.

[61] F Buchthal and H Schmalbruch. "Motor unit of mammalian muscle." In: *Physiological reviews* 60.1 (1980), pp. 90–142.

[62] Dario Farina et al. "The extraction of neural information from the surface EMG for the control of upper-limb prostheses: emerging avenues and challenges". In: *IEEE Transactions on Neural Systems and Rehabilitation Engineering* 22.4 (2014), pp. 797–809.

[63] George Karpati, David Hilton-Jones, and Robert C Griggs. *Disorders of voluntary muscle*. Cambridge University Press, 2001.

[64] Andrew J Fuglevand et al. "Detection of motor unit action potentials with surface electrodes: influence of electrode size and spacing". In: *Biological cybernetics* 67.2 (1992), pp. 143–153.

[65] Hermie J Hermens et al. "European recommendations for surface electromyography". In: *Roessingh research and development* 8.2 (1999), pp. 13–54.

[66] Dario Farina et al. "Standardising surface electromyogram recordings for assessment of activity and fatigue in the human upper trapezius muscle". In: *European journal of applied physiology* 86.6 (2002), pp. 469–478.

[67] Sohee Kim et al. "Thermal impact of an active 3-D microelectrode array implanted in the brain". In: *IEEE Transactions on Neural Systems and Rehabilitation Engineering* 15.4 (2007), pp. 493–501.

[68] Robert F Cleveland and Jerry L Ulcek. "Questions and answers about biological effects and potential hazards of radiofrequency electromagnetic fields". In: *Oet Bulletin*. Citeseer. 1999.

[69] Lantao Huang et al. "Effect of Vertical Metal Plate on Transfer Efficiency of the Wireless Power Transfer System". In: *Energies* 12.19 (2019), p. 3790.

[70] Sebastian Stoecklin et al. "Efficient wireless powering of biomedical sensor systems for multichannel brain implants". In: *IEEE Transactions on Instrumentation and Measurement* 65.4 (2015), pp. 754–764.

[71] Meysam Zargham and P Glenn Gulak. "Maximum achievable efficiency in near-field coupled power-transfer systems". In: *IEEE Transactions on Biomedical Circuits and Systems* 6.3 (2012), pp. 228–245.

Appendix A

Power Transfer Efficiency of Two-coil Links

Consider a two-coil wireless power transfer system consisting of a primary with inductance L_1, parasitic resistance R_1, and resonant capacitance C_1, driven by a source V_s with source resistance R_s. A separate coil (the receiver RX), consists of a primary with inductance L_2, parasitic resistance R_2, and parallel resonant capacitance C_2, terminated with a load resistor R_L.

A.1 Viewed as a Loaded Two-Port Network

Viewed as a two-port network, the power transfer efficiency (PTE) of the link can be found to be:

$$PTE = \frac{Re(Z_L)}{Re(Z_{in})} \frac{|Z_{21}|^2}{|Z_{22} + Z_L|^2}$$

where

$$Z_{in} = Z_{11} - \frac{Z_{12}Z_{21}}{Z_{22} + Z_L}.$$

If Z_{12} and Z_{21} are small, as is the case with loosely-coupled implanted systems, then $Z_{in} \approx Z_{11}$. Thus, under resonance the PTE simplifies to:

$$PTE \approx \frac{Re(Z_L)}{Re(Z_{11})} \frac{|Z_{21}|^2}{|Z_{22} + Z_L|^2}$$

$$PTE = \frac{R_L}{R_{22} + R_L} \frac{|Z_{21}|^2}{R_{22} + R_L} \frac{1}{R_{11}}$$

$$PTE = \frac{R_L}{R_{22} + R_L} \frac{|Z_{21}|^2}{Im(Z_{11})Im(Z_{22})} \frac{Im(Z_{11})}{R_{11}} \frac{Im(Z_{22})}{R_{22} + R_L}$$

$$PTE = \eta_{RX} K^2 Q_{TX} Q_{RX,L}$$

where η_{RX} is the RX efficiency due to loading, K is the coupling coefficient (including both real and imaginary parts of Z_{21}, unlike $k = \frac{M}{\sqrt{L_{TX}L_{RX}}}$ which only accounts for the imaginary part of Z_{21}), Q_{TX} is the TX quality factor, and $Q_{RX,L}$ is the loaded RX quality factor.

Note that the above only holds true under resonance; i.e. when $Im(Z_{22} + Z_L) = 0$. Otherwise, $|Z_{22} + Z_L|^2 \neq (R_{22} + R_L)^2$.

The equivalent load resistance R_L on the RX coil is determined by the supply voltage and power dissipation of the implant as $R_L = \frac{V_{RX}^2}{P_{RX}}$. For the case of an implanted EMGNode, $V_{RX} = 1.8V$ and $P_{RX} = 2mW$, so $R_L \approx 1.5\,\mathrm{k}\Omega$. Plugging this into the expression for $Q_{RX,L}$ results in an effective quality factor close to 0 and an extremely low PTE. In order to rectify this, the load resistance is typically transformed by a parallel resonant capacitor C_2 such that $R_{L,eq} = \frac{(\omega L_2)^2}{R_L}$, thus decreasing the equivalent value and improving the efficiency. Refer to [31] for further discussion.

A.2 Two-Port Efficiency from S-Parameters

The two-coil link can be transformed into a π network with mutual inductance M, and primary/secondary inductances of $L_1 - M$ and $L_2 - M$ respectively. Again assuming ideal complex conjugate matching at input and output, the efficiency is governed by the maximum achievable gain (MAG) which is defined as:

$$MAG = \frac{|S_{21}|}{|S_{12}|}(K - \sqrt{K^2 - 1})$$

where K is the Rollet stability factor given by:

$$K = \frac{1 + |S_{11}S_{22} - S_{12}S_{21}|^2 - |S_{11}|^2 - |S_{22}|^2}{2|S_{12}S_{21}|}$$

MAG can be expressed in terms of Z parameters as:

$$\begin{aligned} MAG = \frac{1}{Re(Z_{12})^2 + Im(Z_{12})^2}(&2Re(Z_{11})Re(Z_{22}) + Im(Z_{12})^2 - Re(Z_{12})^2 \\ &- 2\sqrt{(Re(Z_{11})Re(Z_{22}) - Re(Z_{12}))(Re(Z_{11})Re(Z_{22}) + Im(Z_{12}))}) \end{aligned} \quad \text{(A.1)}$$

For a two-coil link as described above and assuming operation in a non-lossy medium (e.g. air), $Re(Z_{ii}) = R_i, Im(Z_{ii}) = \omega L_i, Im(Z_{12}) = \omega M_{12}$, and $Re(Z_{12}) \approx 0$. Inserting those into the above equation yields the following formula for efficiency in terms of χ:

$$\eta = \eta_{amp}\frac{\chi}{(1 + \sqrt{1 + \chi})^2} \text{ where } \chi = \frac{\omega^2 M_{12}^2}{R_1 R_2} = k^2 Q_1 Q_2.$$

There are two crucial things to note concerning the above analysis. Firstly, the assumption that $Re(R_{12}) \approx 0$ does not hold when the coils are placed in a lossy medium such as the

human body. In this case, the non-simplified expression in eq. (C.1) should be used, which takes into account tissue dielectric losses. Secondly, the analysis assumed ideal complex conjugate matching conditions, which cannot be guaranteed in an application where the secondary load changes (as is the case with "smart" implanted electronics which can have many operational modes with varying power dissipation and therefore varying load impedance). Under these conditions, the load cannot be transformed to the optimal load given by:

$$R_{L,opt} = \sqrt{\frac{R_2}{R_1}(R_1 R_2 + \omega^2 M_{12}^2)}$$

$$|X_{L,opt}| = \omega L_2$$

Refer to [70] for further discussion.

A.3 Viewed as an Optimally-Loaded Two-Port Network

Assume matching exists at both input and output of the two-port network which transform the source resistance R_s and load resistance R_L to the optimum loads for power transfer in the two-port. With this, the two-port efficiency can be defined as:

$$\eta = \eta_{amp} \frac{\chi}{(1 + \sqrt{1 + \chi})^2}$$

where

$$\chi = \frac{|Z_{12}|^2}{Re(Z_{11})Re(Z_{22}) - Re(Z_{12})^2}$$

χ for a traditional two-coil link is given by $\chi = \frac{\omega^2 M^2}{R_1 R_2} = k^2 Q_1 Q_2$. Substituting into the above expression for η gives

$$\eta = \frac{k^2 Q_1 Q_2}{(1 + \sqrt{1 + k^2 Q_1 Q_2})^2}$$

which exactly matches the expression found in the previous section. See [71] for further discussion.